Available online at www.sciencedirect.com

ScienceDirect

Procedia CIRP 113 (2022) 611–635

www.elsevier.com/locate/procedia

21st CIRP Conference on Electro Physical and Chemical Machining (ISEM XXI)

Novel Advances in Machine Tools, Tool Electrodes and Processes for High-Performance and High-Precision EDM

Eckart Uhlmann[a,b], Mitchel Polte[a,b], Sami Yabroudi[a]

[a] *Technische Universität Berlin, Institute for Machine Tools and Factory Management, Pascalstrasse 8-9, Berlin 10587, Germany*
[b] *Fraunhofer Institute for Production Systems and Design Technology, Pascalstrasse 8-9, Berlin 10587, Germany*

* Corresponding author. Tel.: +49-030-314-23349; Fax: +49-030-314-25895. *E-mail address:* eckart.uhlmann@iwf.tu-berlin.de

Abstract

High-performance electrical discharge machining (EDM) is a key technology for manufacturing high-precision components in a broad range of industrially relevant applications. Formation of debris in the working gap leads to arcing and short-circuits on the surface as well as related inaccuracies and process instabilities. Despite decades of research in the field of EDM excessive tool wear and limited process performance are still challenging. In order to overcome highly complex state-of-the-art challenges, dedicated processes, machine tools, peripheral systems, software, tool electrodes and technologies for the application of alternative dielectric fluids have been developed. Within this work novel advances in the development of a sophisticated dry EDM machine tool, including generator and process control technology based on open architecture, open source software, and commonly available machine tool components, are presented. Solutions for challenges regarding remaining debris and gas bubbles as well as related arc discharge and short-circuit pulses in sinking EDM are presented by new flushing methods, technologies and devices. A new system for inverted pressure flushing of a dielectric fluid in ED-drilling enables a highly efficient removal of debris and gas bubbles through the interior channels of the tool electrode. A new multi-fluidic spindle system for EDM provides the ability to use performance- and material-related application of gaseous, near-dry and liquid dielectric fluids sequentially within a single machining process. Recent advances in tool electrode design, tool electrode material application, modification and production have led to essential process improvements. A helical tool electrode design significantly improved flushing conditions and related material removal rate in ED-drilling. Modification of ED-drilling tool electrode surfaces by thermal oxidation of copper reveals a promising approach to minimize ineffective discharges. Application of a specific mesophase-pitch carbon fiber with a diameter of $d_f = 10$ µm using a new process and handling technology enabled drilling holes with a diameter of $d_h = 25$ µm. Next to the shown advances in EDM, efficient development of new process technologies could be enabled by using a specially adapted natural analogue algorithm software tool.

Keywords: Electrical discharge machining (EDM); precision; manufacturing; material removal; tool geometry; micro machining; simulation; spindle; machine tool; machining; heat treatment; process control; algorithm; surface modification; fluid; finishing; optimization; productivity; additive manufacturing

1. Introduction

Electrical discharge machining (EDM) is typically applied for the efficient cutting of complex geometries in hard-to-cut-materials in a wide range of industrial applications. The EDM principle is based on an electro-thermal removal mechanism caused by electrical discharge impulses. Consequently, any material with an electrical conductivity of $\kappa \geq 0.01$ S/cm can be machined. EDM is a key technology for precision manufacturing of complex 3D micro-features and micro-components in difficult to machine and brittle-hard materials such as ceramics, cemented carbides, tool steels, super alloys and titanium alloys. This includes e.g. high-precision tools, molds, injection nozzles and other high-precision structures used in tool making, plastics processing, medical, automotive or aerospace industry [1, 2].

10.1016/j.procir.2022.10.080

Nevertheless, the EDM process and its detailed physical principle are still not fully understood despite of a great number of research activities in the last decades.

The mechanism of EDM in removing small amounts of material by electrical discharges leads to the accumulation of process residuals like debris particles and gas bubbles in the working gap between the tool and the workpiece electrode. Formation of debris in the working gap results in arcing and short-circuits on the surface and subsequently, in related inaccuracies and process instabilities. To maintain stable machining, it is crucial to effectively remove debris particles from the working gap in order to prevent the concentration of discharge locations and related process inefficiencies. This is especially true for sinking and drilling EDM applications, as processing usually takes place in bottom-closed cavities, where debris particles are most likely to accumulate. Consequently, sufficient debris removal besides a precise process control is one of the remaining major challenges in EDM and thus the focus of various research activities in the last decade. Relevant investigations and advances in these fields of work are depicted in the following and serve as a basis for recent advances in machine tools, electrodes and processes presented in chapter 2.

Regarding the application of active flushing in sinking EDM, flushing the working gap merely from one side increases the density of debris particles in the downstream. This results in a varying working gap width s and therefore related inaccuracies [3]. The most efficient flushing methods in sinking EDM and drilling EDM are pressure or suction flushing through holes in the tool or workpiece electrode [4, 5].

Computational fluid dynamics (CFD) simulations in sinking EDM revealed the amplitude of the electrode jump movement A_{max} and its velocity v_{max} as the most important factors for debris evacuation. The presence of bubbles increases the evacuation by up to 46 %, depending on the bubble size [6].

In drilling EDM, high aspect ratios φ reduce the efficiency of flushing and in consequence, the material removal rate (MRR) $\dot{V}_W$ and increase the recast layer thickness d_r. The recast layer is a key limiting factor of drilling EDM applications in aerospace. Furthermore, applying water as dielectric fluid creates smaller bubbles compared to oil and therefore interferes less with the erosion process [7].

In CFD simulations of drilling EDM conditions, the internal flushing channel diameter d_i showed a significant effect on flushing speed v_f and therefore a relevant effect on the efficiency of debris particle removal [8].

Various research has been realized in observing discharge phenomena like consecutive discharges, discharge locations and bubble volume fractions. Within these investigations a relevant dependency between bubble formation and discharge location could be identified [9]. By applying a transparent single crystal electrode and a high-speed camera in sinking EDM investigations, it was found that the working gap is mostly filled with gas bubbles. Consecutive discharges most likely occur in liquid, least in gas and intermediate at the gas bubbles boundaries [10, 11]. In micro-ED drilling, debris particles are not freely distributed but behave colloidal and form clusters. Increasing the discharge frequency f_e adversely affects the process conditions by an excessive generation of gas bubbles [12].

Initial work with gaseous dielectric fluids proved its applicability for stable processing, but also showed contrasting results regarding material removal rate (MRR) $\dot{V}_W$, electrode wear rate (EWR) $\dot{V}_E$ and scatter of molten and reattached material. Single pulse discharge experiments verified the general dispensability of liquid dielectric fluids to remove material from the workpiece electrode, but also revealed that a much higher percentage of generated debris particles in gas reattach to the workpiece surface than in liquid dielectrics because they have not been cooled down sufficiently for solidification [13, 14].

Beyond that, gaseous dielectrics have remained in the focus of research in recent years. The consequences of replacing liquid dielectrics by gases are a reduction of the dynamic viscosity η, an increase of the flow velocity c in the working gap for similar flushing pressures p_f, independence of the machine tank and possible machining in previously unrealizable positions. The use of gaseous dielectrics for EDM therefore promises great advantages in terms of handling, e.g. the gases themselves are not hazardous or flammable and do not need deionization.

Process conditions with liquid dielectrics are significantly influenced by their dynamic viscosity η. The lower the dynamic viscosity η in micro-EDM, the higher the ability of the medium to effectively remove debris and process heat Q as well as the better the surface quality and contour accuracy of the manufacturing results. Low-viscosity dielectrics therefore increase process stability s_p and dimensional accuracy as well as reduce surface roughness and EWR. The intensity of the discharge channel contraction and thus energy density w_e or in the process sequence MRR increase with increasing dynamic viscosity η of the dielectric. With regard to the characteristics of discharges, the main difference between gases and liquids is the density of the medium in which the plasma channel breaks down. A higher density of liquids makes the breakdown more difficult, i.e. a stronger electric field is necessary. In addition, the breakdown mechanism of the plasma channel in gases differs for small working gap widths in the order of $s = 5$ µm. In general, the breakdown mechanism is described by the Townsend electron avalanche theory and is represented by what is known as Paschen's law. In the case of air as dielectric with working gap widths $s \leq 5$ µm and open circuit voltages $\hat{u}_i \leq 360$ V, there is a discrepancy to Paschen's law and the breakdown no longer occurs through ionization of the dielectric as usual, but through ion-enhanced field emission [15, 16, 17]. Fundamental analyses of discharge plasma in liquid and gaseous dielectrics showed that plasma in air is mostly made up of electrode material, whereas in liquids plasma contains constituents originating from the dielectric [18]. For these reasons, process enhancements in dry EDM require different measures than conventional EDM [15, 19]. The scattered, reattached material remains one of the challenging factors in dry EDM [20, 21]. However, an ultrasonic bath with diluted citric acid sufficiently enables the removal of the molten material [21].

Besides experimental studies to increase knowledge about EDM, numerical methods have been established for the modeling of isolated phenomena, aiming at a generalized model for EDM processes. HINDUJA AND KUNIEDA [22] gave

an extensive review over sub-models for simulating different phenomena of EDM and electrochemical machining processes, including flushing, bubble formation, debris movement, energy distributions, discharge plasma, material removal and probabilistic models to determine the discharge locations. Generally, modelling of EDM and its thermal material removal is complex due to the multi-physical nature of the EDM process enclosing various physical and chemical interactions [23].

The aforementioned research and other findings led to the development of additional devices and peripheral systems in order to improve EDM process results. Piezoelectric supported devices are a major focus of several research activities.

KUNIEDA ET AL. [24] developed a piezoelectric system for process optimization in dry EDM with the aim of controlling the working gap width s in dry EDM for improved working gap conditions. They presented a piezoelectric actuator with a high frequency response, resulting in reduced short circuiting and an improved MRR by 70 %. A piezo module based on statistical analyses to control the frontal working gap increased the MRR by 126 % and reduced the EWR by 32 % [25]. A piezoelectric driven EDM head for micro-drilling EDM enabled an orbital motion of the X- and Y-axis. This motion increased the MRR and allowed different hole diameters d_h, independent of the tool electrode diameter d_{el} [26]. A self-regulative system for micro-EDM based on a piezoelectric actuator reacts on the discharge conditions by moving the workpiece electrode against the machining direction. Doing this, deionization and flushing in the working gap as well as process stability s_p improved by eliminating short-circuits [27].

Machining of seal slots in nickel-based alloys was also significantly improved by applying piezo actuators for vibration assisted sinking EDM [28]. The vibration of the tool electrodes generated a passive flushing effect, which improves EDM processing especially for increased machining depth d_m.

This basic principle is applicable as well with ultrasonic vibrations. In micro-EDM experiments, the feed rate v_f could be increased by more than 160 % and machining with an open circuit voltage as low as $\hat{u}_i = 16$ V and stray capacitances C_s was successfully enabled by exciting the dielectric [29]. In drilling EDM an ultrasonic actuation of the tool electrode reduced the machining time t_{ero} by 58 % while obtaining the best hole conicity α [30].

Besides stabilizing the EDM process with improved flushing conditions, process monitoring and control have a major role. An anomaly detection in EDM processing identified disadvantageous process conditions and consequently improved process monitoring [31].

Another approach for improving process performance can be found in the tool electrodes themselves. Tool electrode materials benefit from a high electrical conductivity κ, thermal conductivity λ and specific heat capacity c_p as well as a high melting temperature ϑ_m due to the thermal removal mechanism of EDM [4, 32]. Correlations between different material characteristics like grain size d_g and target parameters of the process like MRR and EWR have been recorded as relevant [33].

Some research activities focused on the structure and design of tool electrodes. A tool electrode apparatus with multiple tubular elements assembled for the roughing operation in sinking EDM enabled active flushing by pumping dielectric fluid into the working gap. In addition, the segments could be moved relative to the workpiece to manufacture different geometries [34]. In more recent research, bundled-tubular and solid tool electrodes were compared. A solid tool electrode provided a 45 % higher MRR than a bundled tool electrode [35].

TRYCH-WILDNER AND KUDLA [36] researched carbon fibers for micro-EDM to qualify them as tool electrodes to manufacture small holes with hole diameters of $d_h < 20$ µm. Using a specially prepared tin solder tool holder, experiments with single carbon fibers led to different formulas describing the EWR but also remaining difficulties in handling and operation [37].

Application of tool electrodes produced by additive manufacturing (AM) in sinking EDM is investigated in several publications [5 ,38, 39, 40]. Experimental analysis of AM copper tool electrodes in sinking EDM revealed that a heat treatment of these tool electrodes enabled processing results similar to conventional copper tool electrodes. Additional use of interior flushing significantly enhanced high aspect ratio machining [41].

The previously shown investigations represent only a limited selection, but reveal great advances in EDM processing. Nevertheless, the EDM process with its enormous complexity still provides numerous further possibilities for improvement. Some of them, including application of novel tool electrode concepts, materials as well as optimization methods and devices are introduced in the following passages.

2. Advances in machine tools, electrodes and processes

2.1. Machine tools, peripheral systems and software

2.1.1. Machine tool for dry EDM

According to the current state of the art, the use of dry-ED milling in micro-production has not yet found its way into practice. This can be explained both by the lack of suitable machine tools for dry-ED milling and by the very few technological studies available. Challenges like precision cutting of brittle-hard materials with corrections of just a few microns, where plastic and elastic deformations affect the chip formation, could be addressed by dry-ED milling. The majority of machine tools available on the market for milling EDM are only suitable for the use of liquid dielectrics. To overcome limitations of deionized water or hydrocarbon-based dielectrics like the favor of workpiece corrosion or flammability, problematic disposal as well as hazardous gases, dry EDM may play a key role. In particular, different pure gases have special advantages in terms of their preferred use for roughing or low-wear finishing. Future success of the use of dry EDM in micro-production in general and dry-ED milling specifically is closely linked to the performance of available machine technology, whose research and development is therefore of central importance. Significantly changed machine requirements arise in particular with regard to the generator and control technology. Technological investigations carried out to date have been realized exclusively using conventional generators, which are not designed for EDM using a gaseous dielectric. Since significantly smaller working gap widths $s \leq 6$ µm occur when using a gaseous dielectric rather than liquid dielectrics, the machine control system must react much more sensitively

to the course of the process. This also has an effect on the required dynamics of the traverse movements of the machine axes that execute control signals. The machine axes used must have both high dynamics and high precision in order to be able to efficiently and precisely control the working gap between workpiece and tool electrodes [17]. With the objective of fulfilling these demands, a machine tool with dedicated machining technology has been developed, see Fig. 1 [17, 42, 43, 44].

The generator technology combines variability and controllability of the static generator with a high discharge frequency f_e and low discharge energies W_e of the relaxation generator. Basically, the generator delivers high-frequency, pulsed current and voltage signals. Individual pulses are realized as isoenergetic discharges. Premature and undesired discharges of the not yet fully charged capacitors are avoided, despite the adverse flushing conditions caused by the very small working gap width s.

The built-in diode prevents the occurrence of secondary discharges in the working gap in the case of an effective discharge and in the case of a higher open circuit voltage $\hat{u}_i$. This prevents transistor failure during continuous operation. Additionally, the discharge process is controllable and risk of failure is minimized. The generator thus enables a constant and predictable discharge energy W_e and discharge frequency f_e. Discharge current i_e, which is controlled by a current limiting module, takes on an almost rectangular shape, which is similar to the pulse shape of static pulse generators.

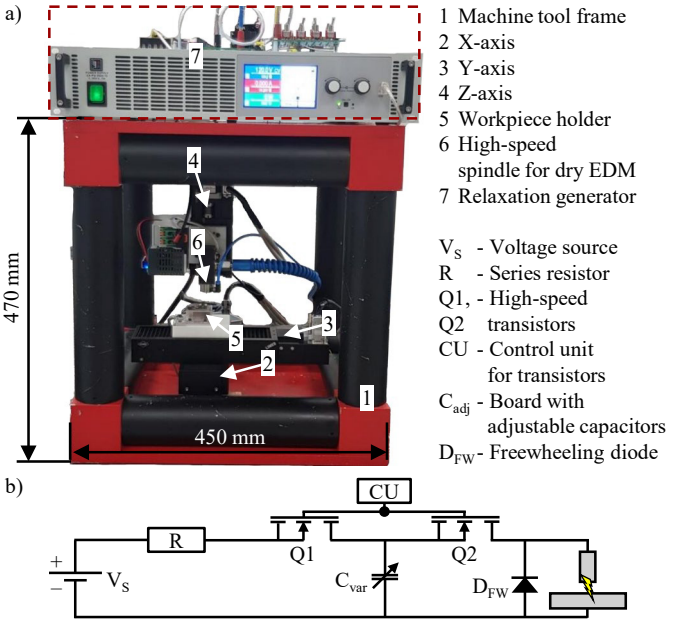

Fig. 1. (a) Machine tool for dry EDM; (b) relaxation generator especially designed for dry EDM.

In contrast, when using a conventional relaxation generator for dry EDM, a quasi-static discharge can be observed as the dominant discharge phenomenon. This has not yet been classified in this form in literature. It shows similarities to a classical relaxation discharge at the beginning, whereas towards the end a behavior like static discharge can be observed, since the current i corresponds to the charging current i_C, Fig. 2.

This can be explained by the very small working gap width s and the insufficient flushing efficiency I_f of the air, which prevents the plasma channel from collapsing after the relaxation discharge and allows the current i from the still connected current source to directly flow through the plasma channel [17, 21]. For this reason, conventional relaxation generators cannot deliver low-energy relaxation discharges for dry EDM due to their design.

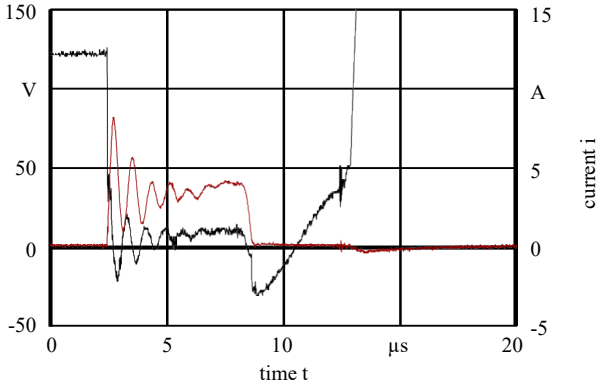

EDM machine tool:
Quadratron 1 with generator AT Spirit 2, GF MACHINING SOLUTIONS, Switzerland
Workpiece electrode:
PMHS 6-5-4 (1.3361)
Processing parameters:

Open circuit voltage	$\hat{u}_i$	= 120.00 V	
Discharge capacity	C_e	= 10.12 nF	$_{el}$ = 0.2 mm
Charging current	i_C	= 5.00 A	
Ontime	t_{on}	= 4.90 µs	
Offtime	t_{off}	= 4.90 µs	$_f$ = 5.0

Fig. 2. Oscilloscope measurement of voltage u and current i of a quasi-static discharge.

The empirical model of the working gap width s for dry EDM in Fig. 3 served as a basis for the selection of suitable actuators for the feed units of the machine tool and the design of an adequate control strategy [42, 43, 44].

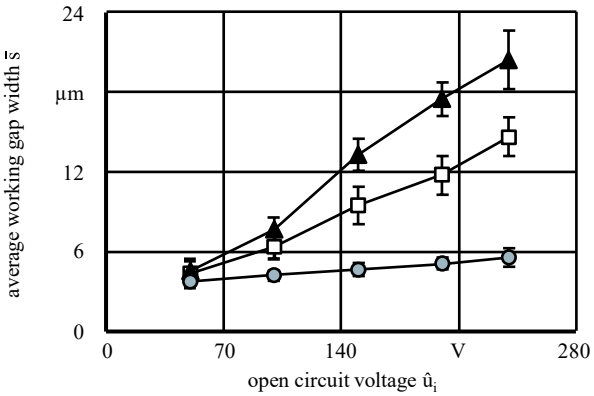

Tool electrodes:
Cemented carbide
Electrode diameter d_{el} = 0.20 mm
Workpiece electrode:
PMHS 6-5-4 (1.3361)
Processing parameters:
Discharge capacity C_e = 10.12 nF
Polarity negative

Dielectric fluid:
▲ Deionized water
Specific conductivity κ = 5.5 µS/cm
□ Hydrocarbon-based dielectric IonoPlus IME-MH, OELHELD GMBH, Germany
○ Compressed air

Fig. 3. Empirical model of the working gap width s in dependence of the open circuit voltage $\hat{u}_i$ when using hydrocarbon-based oil, deionized water or compressed air as dielectric [17].

A spindle for dry EDM enables the use of rotation. It consists of a compressed air-driven dental turbine of type NPA-TU03 from NAKANISHI INC., Japan, with a maximum rotational speed of n = 400,000 1/min, Fig. 4 [44, 45].

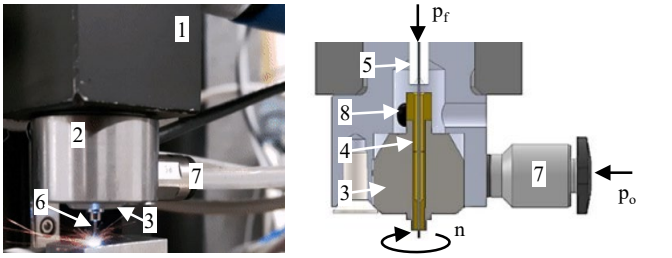

1	Pressure chamber	5	Ceramic sealing	n	Rotational speed
2	Spindle housing	6	Electrode	p_o	Operating pressure
3	Air turbine	7	Air pressure connection	p_f	Flushing pressure
4	Tool holder	8	Sliding contact		

Fig. 4. Spindle for dry EDM, developed by the IWF of the TU BERLIN.

Fig. 5 shows combined results for a cavity machined in full cut mode as well as numerical evidence for the occurrence of debris depositions based on highly compressible real gas CFD and coupled discrete element method (DEM) calculations.

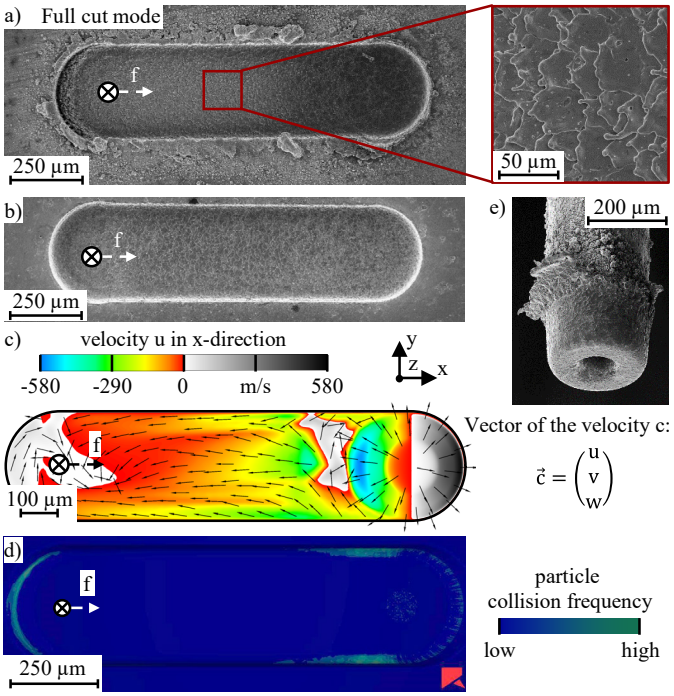

Experimental setup			Numerical setup	
Tool electrodes:			**Software DEM:**	
Cemented carbide			ROCKY DEM 4.5, ESSS, Brazil	
Electrode diameter d_{el} =	300 µm		**Software CFD:**	
Workpiece electrode:			Fluent 2019R2, ANSYS Inc., USA	
PMHS 6-5-4 (1.3361)			Turbulence modeling	SST
Sinking depth d_s =	100 µm		Equation of state (real gases)	Peng-Robinson
Main parameters:			Thermal conductivity λ	Eucken
Rotational speed n =	200,000 1/min		Dynamic viscosity η	Riggs
Flushing pressure p_f =	4 MPa		Specific heat capacity c_p	Polynom
Feed f	process dependent			

Fig. 5. Scanning electron microscope (SEM) images and simulation results of a cavity in full cut mode; (a) after machining; (b) after post-treatment; (c) CFD results: velocity u in x-direction and normalized velocity vectors in top view; (d) coupled CFD-DEM results: particle collision frequency on cavity walls; (e) tool electrode after machining [21].

The reattachment of molten material is visible on the surfaces inside and outside of the cavity as well as on the outer surface of the tool electrode used, Fig. 5 a) and e) [21]. The flow field in Fig. 5 c) is in excellent agreement with the scaly texture in Fig. 5 a). Despite the very high velocities c, the cooling effect of air is not sufficient to directly solidify the recently ejected material. However, the fluid flow forces the still molten material on the surface of the cavity in a backward axial direction. A one-way coupling of CFD and DEM between ANSYS Fluent 2019R2 and ROCKY DEM 4.5 using the calculated compressible 3D flow field provides further insides in the particle trajectories and their collision locations inside the cavity, Fig. 5 d). Finally, the highly complex correlations of the most important fluid mechanic and thermodynamic parameters are visualized for dry EDM for the first time in Fig. 6, post-processing the configuration of Fig. 5.

As a result of the laws for supersonic flows, the highest velocities c occur directly at the transition between the frontal working gap width s_f and the free flow area as well as in the lateral working gap width s_l in the feed direction. In the rear region of the rotating tool electrode, two inward rotating vortices are formed along the edges of the cavity, which detach upwards [21]. These investigations as well as the machine tool for dry EDM provide the basis for further basic and applied research using gaseous dielectrics, even near-dry EDM or multi-fluidic purposes.

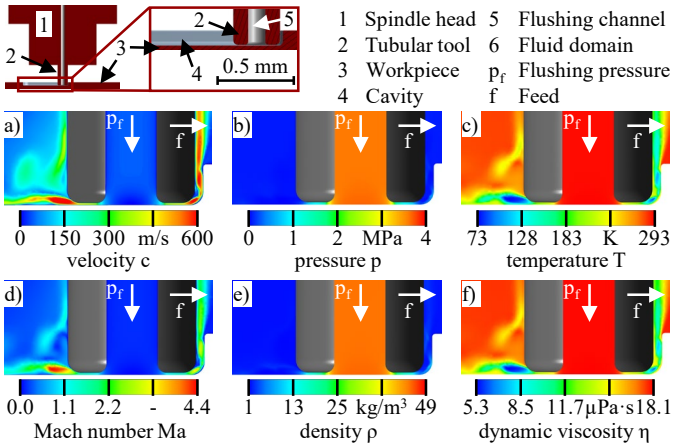

Fig. 6. Effect of compressibility for dry EDM using high-pressure flushing, visualized for different fluid mechanic and thermodynamic parameters; (a) velocity c; (b) pressure p; (c) temperature T; (d) Mach number Ma; (e) density ρ; (f) dynamic viscosity η.

2.1.2. Multi-fluidic spindle for EDM

In EDM, the use of conventional dielectrics has some undesirable disadvantages. For example, carbide formation occurs in ferrous materials under carbon-based dielectrics, where the MRR is significantly reduced. Drilling EDM with deionized water, on the other hand, promises better surface finishes. However, oxidation of the surface layers in ferrous materials causes drawbacks concerning functional surfaces [46, 47].

Gaseous dielectrics have not yet found their way into industry. However, compared to conventional dielectrics, a high MRR can be observed with oxygen and good surface finishes, but a decreased MRR with argon, nitrogen or helium as dielectric, see section 2.3 [47]. Advantages of using gaseous dielectrics and deionized water are opposite to the

disadvantages of hydrocarbon-based dielectrics. For this reason, an approach to enable the combined use of different or mixed dielectrics in order to achieve a possible increase in productivity P of drilling or milling EDM is presented. This allows for an extensive investigation of a combined or even mixed use of different dielectrics with different aggregate conditions in EDM, that is hardly existent today. These investigations aim at lifting potentials of available dielectrics, like combining roughing technologies for drilling low-aspect ratio holes based on oxygen and finishing technologies based on argon, nitrogen or deionized water.

The developed system consists of a spindle with a mass of just $m = 2.5$ kg, providing a rotational speed in the range of $1{,}000\ 1/\text{min} \leq n \leq 40{,}000\ 1/\text{min}$, Fig. 7, with its periphery, including pressure stages, a flexure hinge-based expansion system and a counter pressure device.

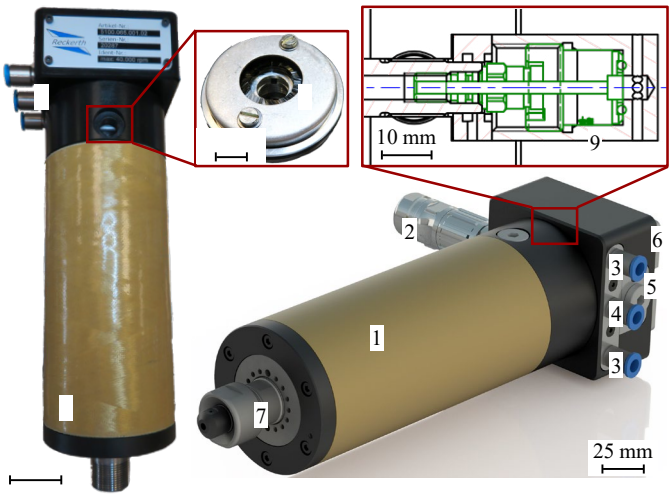

1 Housing, aramid fibre-reinforced
2 Electrical connector
3 Water cooling inlet
4 Sealing air
5 Dielectric supply
6 Connection system 3R
7 Drive shaft with connection
8 Carbon fibre sliding contact
9 Rotary union

Fig. 7. Spindle for multi-fluidic EDM; (a) photographs; (b) CAD.

The special aramid fiber-reinforced composite allows the mass m of the housing to be reduced by 50 % compared to aluminium, while at the same time providing improved mechanical properties as well as good media resistance and very good thermal dimensional stability. The pressure stages enable automatic, continuous and process-dependent switching between the applied dielectrics with the aid of a compact control unit. The control unit uses relevant process signal parameters such as the effective pulse frequency f_e to detect the need to change the dielectric. For this purpose, a compromise is made between detecting high-frequency process instabilities and determining threshold values. A screen enables visualization of process monitoring and manual user input. To reach a flushing pressure of $p_f \leq 80$ bar, an air-driven hydraulic pump with a compression ratio of 1:28 is used. Operating pressure p_o for the pump is provided and set with a proportional pressure control valve. To prevent the dielectric from exceeding flushing pressure p_f and precisely dispensing it, a pressure control valve is installed between the spindle and the pump. Flushing pressure p_f will be continuously measured by a pressure transmitter. The components are connected to a pinboard as well as to a microcontroller board. The latter controls output voltages u_{out} of individual pressure control valves and processes input voltages u_{in} of the pressure transmitter.

Due to the dependence between the working gap width s and the respective dielectric, see Fig. 3, the working gap width s may be increased when dielectrics are switched in the direction of a higher dynamic viscosity η. This increase ensures that flushing volume flow $\dot{V}_f$ can be maintained and is therefore essential for a stable process.

To realize the increase of the working gap width s, a system was developed for eccentric deflection of the tool electrode using a flexure hinge, Fig. 8. Using preloaded stack actuators of type PA 50/T14 from PIEZOSYSTEM JENA GMBH, Germany, a precise and dielectric-dependent variation of the lateral working gap width of up to $\Delta s_l = 40$ µm is enabled.

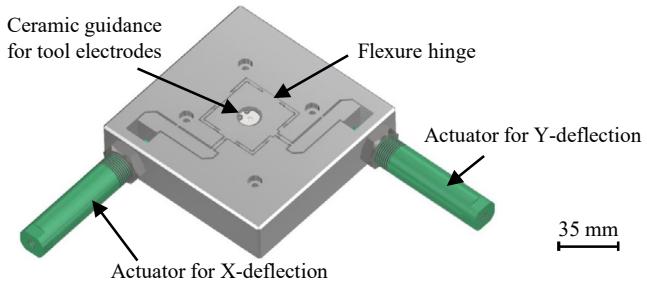

Fig. 8. System with flexure hinge to increase the lateral working gap width s_l.

During machining of through holes by use of pressure flushing in drilling EDM, the dielectric escapes through the first breakthrough, resulting in a pressure loss Δp_l, a decreased flushing volume flow $\dot{V}_f$ in the working gap and consequently a sharp drop of adequate flushing as well as process stability s_p and feed rate v_f. To meet this, a counter-pressure device was developed to establish a back pressure of $p_b \leq 8$ bar and prevent uncontrolled leakage of the dielectric during breakthrough, Fig. 9. As a result, flushing volume flow $\dot{V}_f$, high process stability s_p as well as a high MRR are maintained.

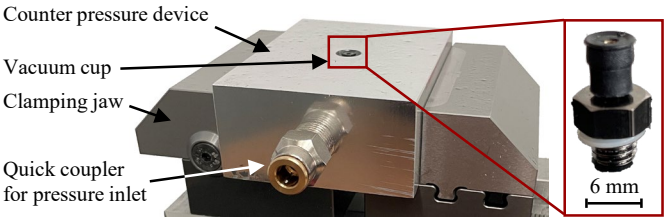

Fig. 9. Counter pressure device to build up back pressure for drilling EDM.

Currently, drilling and milling EDM are carried out on the basis of inflexible and outdated technologies that do not make use of the available technological potential. The spindle for multi-fluidic EDM enables the extension of existing, multi-axis machine tools for EDM by an innovative and dielectric-flexible spindle system.

2.1.3. Inverted pressure flushing

Debris and gas bubbles generated during drilling EDM are typically evacuated by use of pressure flushing via the shape-defining lateral working gap width s_l. Such contaminations have a high potential to bridge the working gap and to result in abnormal discharges, and negatively influence process stability s_p. Different types of discharge events, such as effective discharge pulses, open-circuit pulses, short-circuit pulses and arc discharge pulses or arcing can be classified in

different ways, e.g. normal or abnormal versus effective discharge pulses or less or non-useful power pulses. The latter destabilize the manufacturing process and consequently slow down the feed rate v_f considerably. These events are associated with a decrease of the MRR, an increase of the EWR and deteriorations of the process results in terms of hole conicity α and surface roughness characteristics. Destabilization of process conditions is directly linked to an increasing machining depth d_m, since a decreased flushing efficiency I_f makes evacuation of debris and gas bubbles more difficult [48, 49]. This fact led to various approaches to meet the resulting limited aspect ratios φ in drilling EDM with improved flushing conditions or novel flushing methods.

One of these methods is the inverted pressure flushing method. By using this new flushing method, material removal residuals occurring during the ED drilling process are specifically evacuated by applying a pressure $p \leq 8$ bar inside the pressure chamber, which forces any fluid flow through the interior flushing channels of the tool electrode. Fig. 10 shows the developed pressure chamber for inverted pressure flushing. As part of the investigation, Design of Experiments (DoE) using the Response Surface Method (RSM) and the Box-Behnke design were carried out for further optimization.

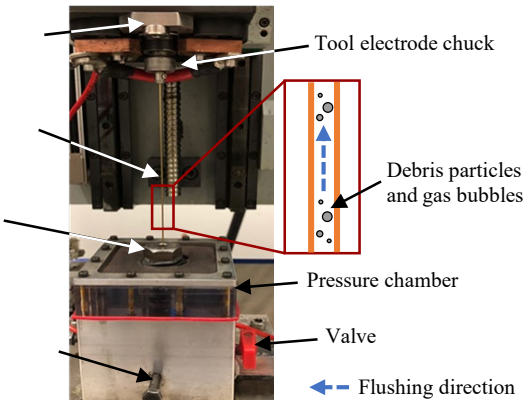

Fig. 10. Developed pressure chamber for inverted pressure flushing.

Using deionized water, an increased MRR in the form of a reduced machining time t_{ero} could be demonstrated with inverted pressure flushing, and a correlation between the direction of flushing and the machining results was verified.

The following Fig. 11 shows the best absolute values of the machining time t_{ero} for machining of through holes with a machining depth of $d_m = 20$ mm in the case-hardened steel X19NiCrMo4 (1.2764) by use of conventional pressure flushing, compared to the use of inverted pressure flushing in three cases: before a 1st DoE as well as after the 1st and after the 2nd DoE. It can be seen that each set of processing parameters for inverted pressure flushing provides better machining times t_{ero} than conventional pressure flushing. Machining time was reduced from $t_{ero} = 1{,}164$ s, with the conventional flushing method to $t_{ero} = 558$ s and with inverted pressure flushing after the 2nd DoE.

As can be seen, the machining time t_{ero} could be reduced by 52 % with approximately constant linear wear of the tool electrode Δl_E. Furthermore, the surface roughness Ra inside the bore hole could be slightly reduced by 6 %, down to Ra = 1.05 µm after the 2nd experimental run.

In comparison to conventional pressure flushing, inverted pressure flushing has the capability to foster process stability s_p and to improve target parameters of drilling EDM. For this reason, a controlled add-on module for commercial machine tools for EDM will be developed in order to transfer the inverted pressure flushing method to the industrial practice of drilling EDM. Combining the developed pressure chamber, additional periphery and machining technologies for drilling EDM effectively avoids process-destabilizing effects and shape deviations with potential applications in aerospace and connected industries.

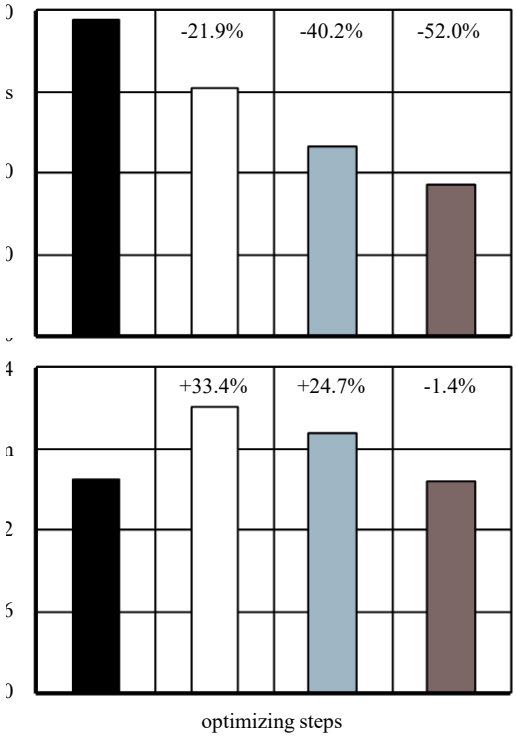

EDM machine tool:
Hybrid drilling system „MicroDrill“ with pulse generator by ZIMMER & KREIM GMBH & CO. KG, Germany
Tool electrode: Brass
Electrode diameter d_{el} = 1.5 mm
Processing parameters:
Discharge current i_e = 17.0 A
Discharge duration t_e = 14.0 µs
Pulse intervall time t_0 = 12.0 µs
Open circuit voltage $\hat{u}_i$ = 190.0 V

Workpiece electrode:
Case-hardened steel X19NiCrMo4 (1.2764)
Machining depth d_m = 20 mm

Pressure flushing
IPF - before 1st DoE
IPF - after 1st DoE
IPF - after 2nd DoE

IPF - Inverted pressure flushing

Fig. 11. Experimental results comparing pressure flushing with inverted pressure flushing, with and without optimized parameters [50].

2.1.4. External automated flushing unit for sinking EDM

Further developments of debris removal by flushing were also carried out in the field of sinking EDM. Compared to drilling EDM, pressure flushing through inner channels is not economically feasible due to increased efforts for individual tool electrode preparation and related inhomogeneous or discontinuous debris removal. Commonly, wire drawing is used to machine inner channels in cylindrical tool electrode geometries, but this is not applicable for more complex geometries. In these cases, other flushing methods like electrode jumps or side flushing have to be used to remove debris from the working gap. Current challenges for side flushing are not yet reproducible machining results due to the

manual alignment of flushing nozzles as well as the lack of a possible integration into automated process chains.

As a solution, an external automated flushing unit has been developed. This flushing unit allows an integration into automated process chains for the first time, as it is able to move automatically out of the processing area. To investigate optimal positions for side flushing, a complex statistical procedure was developed to carry out CFD simulations [51]. An idealized 2D CFD-model for a simple tool electrode geometry was applied to get insights into the fluid dynamics inside and outside of the working gap, Fig. 12.

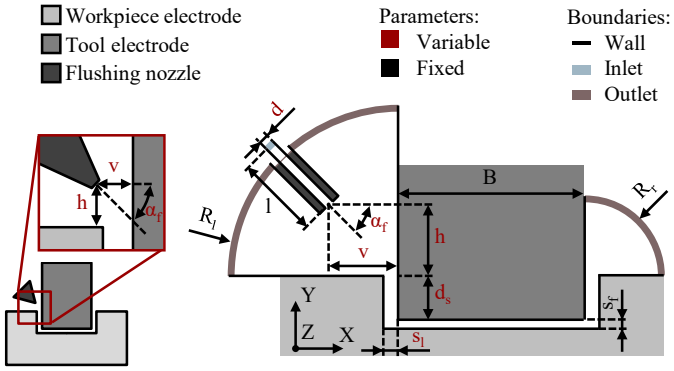

h	Horizontal nozzle position	s_f	Frontal working gap width
v	Vertical nozzle position	B	Tool electrode width
α_f	Flushing angle	R_l	Radius of outlet left
d_s	Sinking depth	R_R	Radius of outlet right
d	Nozzle width	l	Length of nozzle channel
s_l	Lateral working gap width		

Fig. 12. Idealized 2D CFD-model for side flushing simulations.

In these simulations, the horizontal nozzle position h, the vertical nozzle position v, the sinking depth d_s as well as the flushing angle α_f were varied. The volume flow $\dot{V}$ and the velocity c were calculated in the center of the frontal working gap. The considered multidimensional parameter space requires a high number of simulations of $n_{sim} = 1.6 \cdot 10^8$, resulting in an unfeasibly high simulation time t_{sim}. To reduce the high simulation time t_{sim}, metamodels were applied by estimating arbitrary values in the multi-dimensional parameter space. Different DoEs and metamodels have been investigated and compared within the procedure shown in Fig. 13 to identify the most suitable combination and hence, drastically minimize the number of simulations n_{sim}.

Initially, simulations were carried out according to the respective DoE. These results were then used to train metamodels. Subsequently, additional simulations in the intermediate spaces verified the results of the metamodels. Statistical analyses were performed to determine the most successful combination of DoE and meta model with the least percentage error pe of the approximation.

In Table 1, the percentage errors pe such as mean absolute percentage error (MAPE) pe_{MA}, root mean square percentage error (RMSPE) pe_{RMS} and maximal absolute percentage error (MAXPE) pe_{MAX} of different DoEs, such as 3k-design, Generalized Subset Design (GSD) and Latin Hypercube Sampling (LHS), were compared using the simple Kriging regression.

Table 1. Percentage errors pe for investigated DoEs for a sinking depth of d_s = 2mm (simple Kriging regression).

Percentage error pe	3k-design	GSD	LHS
MAPE	18.5 %	100.1 %	12.9 %
RMSPE	26.2 %	167.8 %	20.9 %
MAXPE	117.4 %	783.4 %	103.3 %

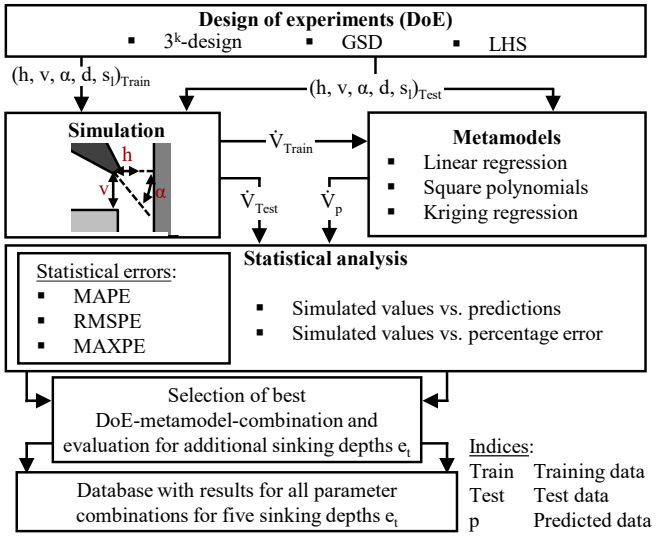

Fig. 13. Procedure of using statistical methods to reduce the number of simulations n_{sim}.

As seen in Table 1, LHS achieved the least percentage errors p_e. Afterwards, the percentage errors pe for LHS were compared for linear regression, quadratic polynomial regression, simple Kriging, universal Kriging with linear function and universal Kriging with quadratic polynomial. The most promising metamodel for LHS was the Kriging regression with quadratic polynomial with a MAPE of pe_{MA} = 3.28 % and a MAXPE of pe_{MAX} = 17.24 %.

In total, the combination of LHS and Kriging regression could reduce the number of simulations n_{sim} by a factor of $F_{n,sim} = 10^6$. Calculated data are stored in a database to directly obtain the optimal position for side flushing in terms of maximum volume flow $\dot{V}_{max}$. Fig. 14 presents an exemplary diagram.

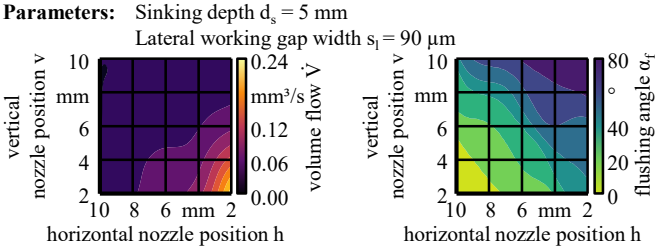

Fig. 14. Volume flow $\dot{V}$ and flushing angle α_f in dependence of the flushing nozzle position.

The simulation in Fig. 14 for a sinking depth of d_s = 5 mm shows that the highest volume flow of $\dot{V}$ = 0.24 mm³/s could be achieved near the lateral working gap with a flushing angle between 40 ° < α_f < 50 °. Horizontal and vertical positions of h < 6 mm and v > 6 mm require a flushing angle α_f > 50 °. For a flushing angle α_f < 40 ° horizontal and vertical positions of h > 6 mm and v < 6 mm are required to obtain sufficient volume flows $\dot{V}$. Experimental trials confirmed similar, but

weak dependencies. These experiments lack certainty, caused by the general disadvantages of physical experiments, like geometry and effort related limitations. In contrast, combining statistical procedure and CFD simulations allows to pre-investigate optimal flushing configurations, even for complex electrode geometries and multiple flushing nozzles.

The development of the flushing unit's design not only considers optimized flushing parameters, but also offers solutions for the challenges of side flushing mentioned before.

The main assembly group containing the flushing nozzle is either positioned at the active machining position or at the standby position, where automated tool or workpiece electrode replacements are not hindered. Independent positioning of the nozzle to the active machining position is ensured by a variety of sensors, such as an ultrasonic sensor, a light barrier, a capacitive and inductive sensor, see Fig. 15.

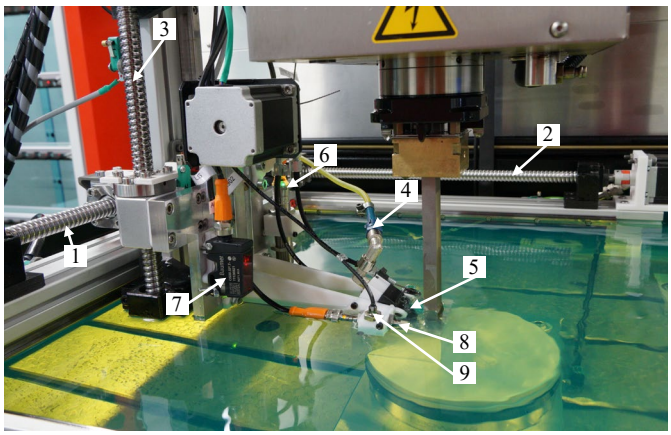

1 X-axis
2 Y-axis
3 Z-axis
4 Dielectric fluid supply
5 Flushing nozzle
6 Ultrasonic sensor
7 One-way light barrier
8 Capacitive sensor
9 Inductive Sensor

Fig. 15. Developed external automated flushing unit in the machine tank.

Positioning of the flushing angle α_f is ensured by fine-step motors. In addition, the geometry and size of the flushing nozzles can be adjusted by changeable nozzles made by additive manufacturing, enabling a local optimization of the flushing process. The present design furthermore allows to use higher flushing pressures $p_f \geq 1$ bar for sinking EDM.

With these features of the external automated flushing unit and detailed insights generated by CFD simulations and statistical methods, further enhancement of the flushing unit by advanced sensors, actuators or programming can be realized. As results of first experimental investigations already indicate, external automated flushing shows the potential to reduce machining times t_{ero} by 40 % and the relative linear wear ϑ_l by 50 % as an addition to or replacement of electrode jumps.

2.1.5. Active redistribution of discharges using segmented tool electrodes

As mentioned in the previous section, in sinking EDM the most common approaches for the removal of debris are of active or passive nature using electrode jumps or side flushing. However, complex electrode geometries and lack of interior flushing channels in most tool electrodes hinder the applicability of these methods [52]. An alternative method to overcome challenges like debris-related process instabilities is the active redistribution of electrical discharges by means of a tool electrode consisting of electrically insulated segments. With active redistribution, discharges can only occur in selected sections of the working gap. Within sections where discharges cannot occur, debris particles can move out of the working gap without causing abnormal discharges.

Fig. 16 shows the basic principle to realize this method. The tool electrode consists of individual segments that are electrically insulated from each other and connected to the EDM pulse generator through switching elements. By periodically switching the electrical connection of tool electrode segments on and off, control of discharge occurrences is enabled. As a result, discharges can only ignite in the frontal working gap below one single tool electrode segment. This decreases the probability of local debris accumulation and hence abnormal discharge events. Local and temporary sequences of consecutive short-circuit pulses or arcing will be interrupted by actively shifting the location of discharge events and material removal, without the need of an electrode jump. It thereby facilitates local deionization of the dielectric fluid as well as removal of debris at those sections of the working gap adjacent to the segments being turned off.

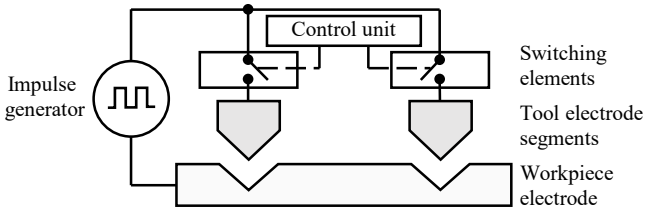

Fig. 16. Basic principle for the purpose of an active redistribution of discharges.

Experiments using two tool electrode segments were carried out by alternatingly switching one segment on while the other one was switched off. The tool electrode segments made of EDM-3 graphite by POCO GRAPHITE INC., USA, had a square cross-section with an edge length of $l_e = 5$ mm. The sinking depth d_s in the workpiece electrode of Elmax Superclean (X170CrVMo18-3-1) was $d_s = 5$ mm [53].

It was found that an active redistribution of discharges led to an increase in MRR of 28 % and a decrease in relative tool wear ϑ by 48 %, from $\vartheta = 1.10$ % to $\vartheta = 0.57$ % as shown in Fig. 17. The relative tool wear ϑ is defined as the ratio of the EWR with the MRR. Furthermore, the edge wear was reduced by 23 % as an edge radius of $r_e = 249$ µm was measured on the segments used with active redistribution compared to an edge radius of $r_e = 326$ µm on the segments used without active redistribution. These results can be considered as verification of the fact that an active redistribution of discharges has locally led to significantly improved process conditions in the frontal working gap, resulting in an increased ignition of effective discharge pulses providing efficient material removal and low wear.

Experiments using a tool electrode made up of electrically insulated segments for an active redistribution of discharges showed promising results. It was observed that switching between two tool electrode segments with a switching interval of $t_s = 100$ ms led to an increased MRR as well as a reduced relative tool wear ϑ. This can be explained with less sequences of open-circuits and abnormal discharges for the 1,333

discharge events within each switching interval, both increasing the proportion of effective discharges or the normal frequency ratio λ_{norm} in the less contaminated dielectric, see section 2.2.2. This way, effective discharge pulses are concentrated and kept in the frontal working gap enabling continuous material removal without interruptions by electrode jumps or abnormal discharges. Short-circuiting and arcing is especially prevented in the lateral working gap, because debris and gas bubbles ascend during periods when their tool electrode segment of origin is switched off. The influence of the switching interval t_s needs to receive further analysis in that regard.

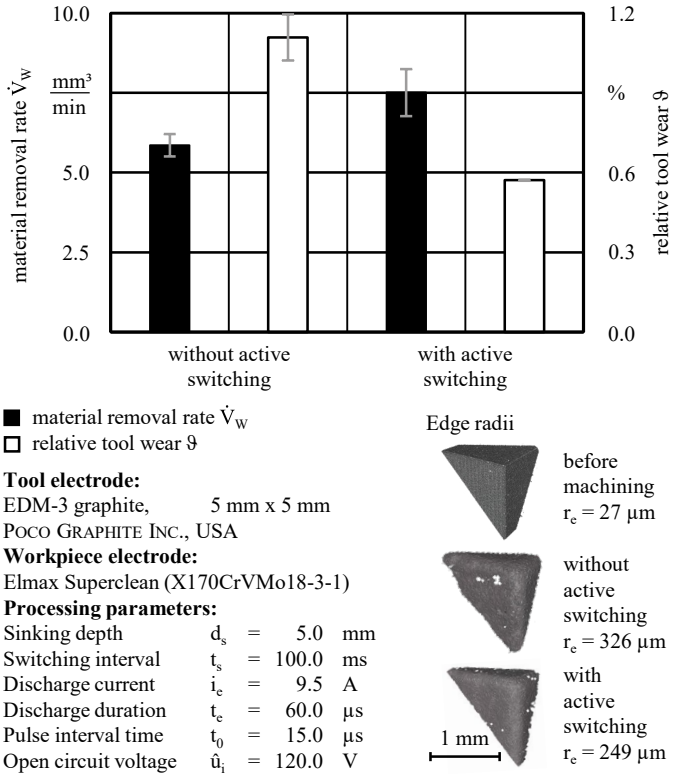

Tool electrode:
EDM-3 graphite, 5 mm x 5 mm
POCO GRAPHITE INC., USA
Workpiece electrode:
Elmax Superclean (X170CrVMo18-3-1)
Processing parameters:

Sinking depth	d_s	=	5.0	mm
Switching interval	t_s	=	100.0	ms
Discharge current	i_e	=	9.5	A
Discharge duration	t_e	=	60.0	µs
Pulse interval time	t_0	=	15.0	µs
Open circuit voltage	$\hat{u}_i$	=	120.0	V

Fig. 17. Experimental results comparing regular EDM with EDM with active discharge redistribution.

In future experiments, the use of a tool electrode made up of up to 25 segments will be investigated. By bonding the segments to each other with an insulating adhesive, the tool electrode can be machined into arbitrary shapes in common process chains. This enables the use of complex workpiece geometries while simultaneously keeping the advantage of active discharge redistribution.

2.1.6. Nature analogue algorithms

At state of the art, the machining of individual material combinations and complex geometries is characterized by the major challenge of elaborating suitable EDM processing parameters caused by non-linear correlations in EDM [4, 54]. According to previous investigations, the discharge energy W_e resulting from the average discharge voltage $\bar{u}_e$, the average discharge current $\bar{i}_e$, and the discharge duration t_e have a significant influence on the target parameters, such as machining time t_{ero} and linear wear of the tool electrode Δl_E.

The stochastic optimization method evolution strategy (ES) generates parameters based on previously determined vectors, called parents μ. Using this as generation, the ES-algorithm generates a probability distribution from which to sample parameter vectors, the children λ. These new parameter vectors are applied in experiments afterwards. The obtained results are analyzed and sorted by the optimization criterion that needs to be defined. In the following step, former children become parents of subsequent generations. Using the (μ, λ)-ES, the parent vector of a current generation is not considered in the selection process. In contrast, in the (μ+ λ)-ES the best child of each previous generation is again part of the next trial. If no significant improvement or a threshold value of the optimization criterion has been reached, ES ends [55]. An ES variant that restarts the algorithm after a certain number of generations using the best parent vector obtained in the preceding generations is called a nested ES. A variant without a restart is called a simple ES.

Within the presented investigations, a simple (1,4)-ES with a simple (1+4)-ES [56] and a nested (1,4)-ES with a nested (1+4)-ES [57] were compared in a first step. Based on these works, two types of ES, a simple (1,4)-ES and a nested (1,4)-ES, were applied afterwards. As part of the variants, a covariance matrix adaptation (CMA) of the probability distribution is applied to the new generation of samples. Starting with the same parent vector of processing parameters in each generation, the simple variant samples four children and calculates their covariance by using the aforementioned covariance matrix. An objective function is used to evaluate the children, and the best child vector is chosen as a parent vector for the following generation. After five generations within the nested variant, the algorithm is restarted. Again, after five generations, the CMA is re-run without any input from the previous covariance matrix. The algorithms used to search for input parameters minimizing the objective function were two variants of the (μ, λ)-ES with CMA by HANSEN [58].

The following EDM processing parameter ranges were considered:

- discharge current between 0.5 A ≤ i_e ≤ 20.0 A,
- open circuit voltage between 80.0 V ≤ $\hat{u}_i$ ≤ 270.0 V,
- discharge duration between 0.5 µs ≤ t_e ≤ 50.0 µs and
- pulse interval time between 0.5 µs ≤ t_0 ≤ 100.0 µs.

As a linear combination of target parameters machining time t_{ero} and linear wear of the tool electrode Δl_E, both were normalized with the respective values of the starting processing parameters. The target parameter machining time t_{ero} is weighted with 70 % and the linear wear of the tool electrode Δl_E with 30 % respectively, because the focus of most drilling EDM applications is on minimizing the machining time t_{ero} as opposed to minimizing the linear wear of the tool electrode Δl_E. The objective function may then be defined as, Eq. 1.

$$f\left(i_e^k,\, \hat{u}_i^k,\, t_e^k,\, t_0^k\right) = 0.7 \cdot \frac{t_{ero}^k}{t_{ero}^0} + 0.3 \cdot \frac{\Delta l_E^k}{\Delta l_E^0} \tag{1}$$

The count of the ES generation is given by the superscript k. If $f\left(i_e^k, \hat{u}_i^k, t_e^k, t_0^k\right) < 1$ the processing parameters result in improved process results. The value of the objective function

for given processing parameters is called quality criterion and denoted by $q_c = f\left(i_e^k, \hat{u}_i^k, t_e^k, t_0^k\right)$.

Fig. 18 a) shows the values of the quality criterion q_c of three executions of the (1,4)-ES over ten generations. Similarly, Fig. 18 b) shows the respective quality criterion q_c for the nested (1,4)-ES.

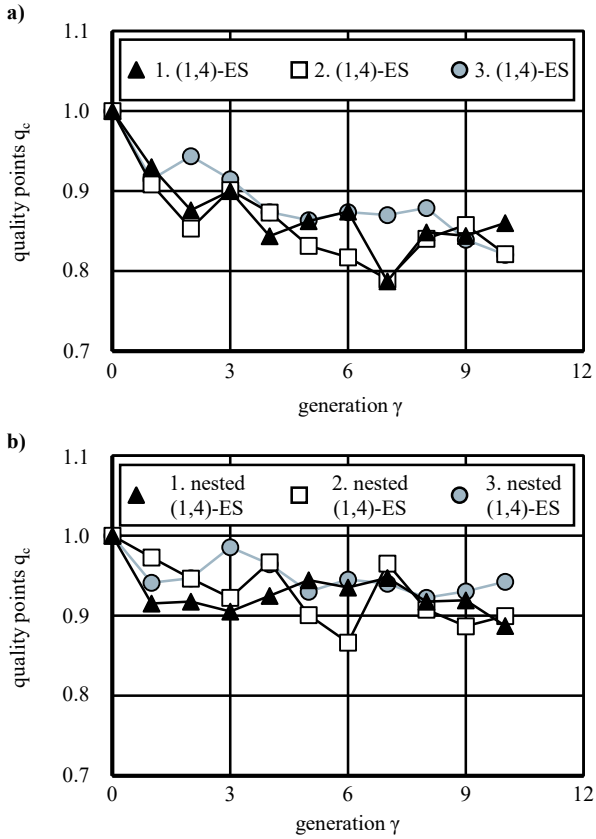

Fig. 18. Quality criterion q_c of all three executions of; (a) (1,4)-ES; (b) nested (1,4)-ES.

The success of the ES in obtaining processing parameter vectors minimizing the objective function's value is illustrated in both diagrams. In the (1,4)-ES, the best child was generated in the seventh generation of the first execution with a value for the quality criterion of $q_c = 0.787$ and an improvement by 22.3 %. In the nested (1,4)-ES, the best child was generated in the sixth generation of the second execution with a value of the quality criterion of $q_c = 0.866$ achieving an improvement by 13.4 %. Compared to the set of parameters of a drilling EDM process, the (1,4)-ES and nested (1,4)-ES resulted in a 40 % and 27 % reduction of the machining time t_{ero}, respectively. The results show that the (1,4)-ES utilizing CMA without reset leads to a better process result than nested (1,4)-ES utilizing CMA with reset. Upcoming investigations will focus on a closed loop process optimization by means of the evolution strategy.

2.2. Tool electrode geometries and materials for sinking EDM and drilling EDM

2.2.1. Variable tool electrode for sinking EDM

In industrial settings, sinking EDM usually requires numerous tool electrodes to achieve the final geometry of a workpiece. Especially in manufacturing high-precision components, the relative tool wear ϑ of single features that are part of a complex tool electrode has to be compensated by repeating process steps to approach or reach a final contour accuracy and surface quality. This results in potentially avoidable high manufacturing times t_m and production costs c for each workpiece.

The presented solution for this specific challenge covers a tool electrode that is divided in several bundled actuated tool electrode segments (ATES), Fig. 19. This enables the flexible shaping of the tool electrode for roughing operations in sinking EDM to produce a specific geometry in a workpiece. The required geometry can be set via the actuators.

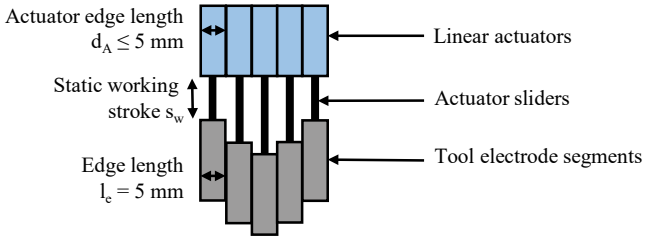

Fig. 19. Concept of the actuated tool electrode module for sinking EDM.

Beyond that, new flushing strategies may be implemented based on oscillating wave movements of the ATES to generate transverse waves in the dielectric fluid [59]. Fig. 20 visualizes the flow of dye infused water for selected points in time, caused by such a synchronized actuation of five ATES.

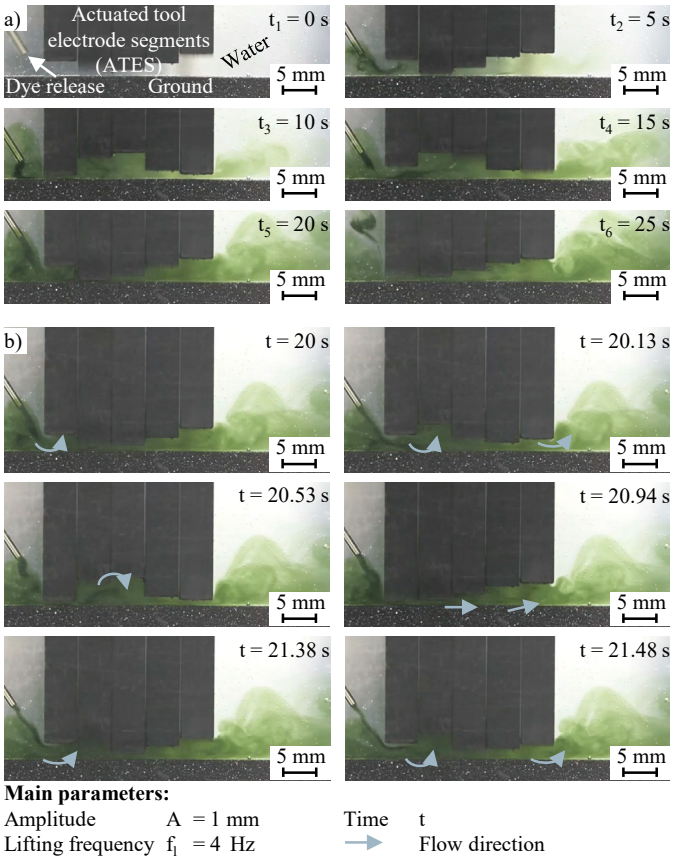

Fig. 20. Transverse waves generated by oscillating tool electrode segments; (a) global flow; (b) local flow pattern.

The dye is released manually and very slowly to keep the impact on the fluid flow as small as possible. Under the influence of local low-pressure regions below each ATES, the

dye infused water follows the sequence of uplifting ATES from left to right to be finally released on the opposite side.

For conceptual implementation together with the MECHATRONIC SYSTEMS LABORATORY EMK of the TU BERLIN, cuboid segments with an edge length of $l_e = 5$ mm are chosen and miniaturized linear actuators with an actuator edge length of $d_A \leq 5$ mm are being developed. Detailed modeling and control of the miniaturized linear drive as well as its implementation in the machine tool as a single ATES was published by SCHULTE ET AL. and UHLMANN ET AL. [60, 61].

In first experiments the process behavior of a single ATES is analyzed during sinking EDM. For this purpose, the MRR and the relative linear wear ϑ_l are measured and compared using different Z-axis lifting motions, namely the actuator, the machine tool and without Z-axis lifting motions as a reference. The developed actuator provides a static working stroke of $s_w = 30$ mm as well as a dynamic excitation with an amplitude in the order of $A = 1$ mm and a lifting frequency of up to $f_l = 10$ Hz. A Hall sensor is implemented in the actuator to detect the position of the slider during machining. The actuator keeps the ATES at a fixed static working stroke s_w for a period of $T_e = 0.7$ s and subsequently realizes a Z-axis lifting motion with an amplitude of $A = 1$ mm for a flushing time of $T_f = 0.1$ s to remove debris and gas bubbles from the working gap. This lifting cycle is similar to an integrated lifting motion or electrode jump of the machine tool, but it allows for external and individual manipulations. The applied roughing technology aims at a sinking depth of $d_s = 5$ mm with a surface roughness of $Ra = 10$ µm, corresponding to a class 40 according to VDI guideline 3400. An insulating coupling is used to secure the tool electrode segment to the slider of the actuator and a 3D-printed mounting bracket is used to attach the actuator to the machine tool.

Fig. 21 shows the results of these experiments for the MRR and the relative linear wear ϑ_l. In the cases of Z-axis lifting motions by the actuator, a significant increase of the MRR by 37 % with a slightly higher relative linear wear ϑ_l could be achieved, compared to the experiments without any Z-axis lifting motion. This improvement is a consequence of better flushing conditions in the working gap.

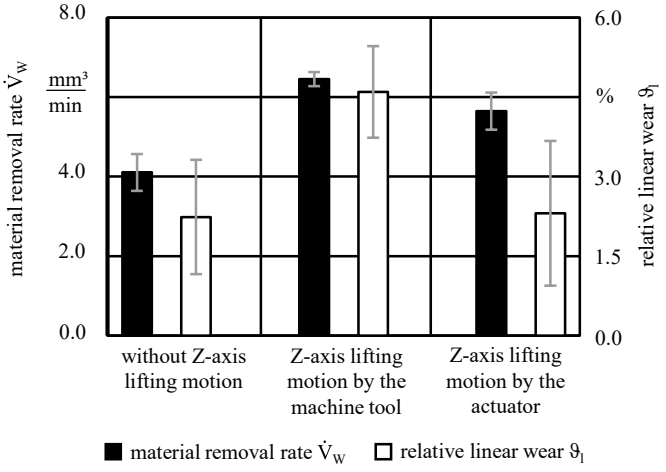

Fig. 21. MRR and relative linear wear ϑ_l for different Z-axis lifting motions [61].

The highest average MRR with $\dot{V}_W = 6.5$ mm³/min occurs at Z-axis lifting motion by the machine tool, along with the highest relative linear wear of $\vartheta_l = 4.6$ %. The actuated Z-axis lifting motion in comparison shows a MRR of $\dot{V}_W = 5.6$ mm³/min and a significantly reduced relative linear wear of $\vartheta_l = 2.3$ %. Reference experiments without any Z-axis lifting motions resulted in a MRR of $\dot{V}_W = 4.1$ mm³/min with a relative linear wear of $\vartheta_l = 2.2$ %.

This conceptual implementation demonstrated the applicability of an ATES for sinking EDM. In the future, multiple ATES will be combined to form an actuated tool electrode module for flexible shaping of tool electrodes. With this system, a new type of flushing strategy that applies transverse waves will be validated for sinking EDM. The machining times t_{ero} will be decreased by a more effective flushing and thus, production costs c can be reduced.

2.2.2. Tool electrodes with exterior flushing channels

In drilling EDM, the rotation of the tool electrode allows to use asymmetric tool geometries while still ensuring roundness of a bore hole. This provides the opportunity to utilize the space, that flutes along the tool electrode's lateral surface provide, for the evacuation of debris and gas bubbles. Also, asymmetric multi-channel tool electrodes have the advantage to mostly avoid pin formation inside blind holes [7]. Most authors focused on passive flushing when applying exterior flushing channels to cylindrical rods in the form of straight slots or helical flutes [49, 62, 63, 64]. Inclined through holes have also successfully been investigated by KUMAR AND SINGH [64, 65], although the manufacturing times of $t_m = 22$ min for each tool electrode most probably foil the advantages. In both works, the aspect ratio φ achievable as well as MRR, EWR and hole conicity α could be improved. Nevertheless, the state of the art still misses holistic observations with focus on the industrial application of tool electrodes with exterior flushing channels. Finally, no interactions with pressure flushing have yet been investigated.

Both rod type as well as single- and four-channel tool electrodes made of brass were investigated for electrode diameters of $d_{el} = 3$ mm. Flutes have been machined in the lateral surface using an automatic CNC lathe, enabling manufacturing times in the order of $t_m = 1$ min. It was found that minimum flute depths of $d_f > 0.3$ mm and flute angles of $\alpha_f \geq 45$ ° are needed to improve the drilling EDM process performance by up to 39 % in terms of the machining time t_{ero} [66]. Table 2 shows six types of tool electrodes for further examination of internal geometries and interactions with exterior flushing channels.

Table 2. Six types of tool electrodes with interior and exterior geometries.

Name	Without exterior flushing	Name	With exterior flushing
R	Rod	HR	Helix rod
1C	Single-channel	H1C	Helix single-channel
4C	Four-channel	H4C	Helix four-channel

The worn tool electrode tips of these types of tool electrodes without and with exterior flushing channels differ in their contour. The radial wear and reattached molten material of the tool and workpiece electrode may remove or clog the start of the flute for flute angles of $\alpha_f < 45$ ° and flute depths of $d_f \leq 0.3$ mm. Also, cavities pointing inwards are formed at the tool electrode tips of rod type tool electrodes. These cavities

are caused by stationary vortices at the bottom of the borehole that result in a frontal accumulation of debris, inducing locally increased relative tool wear ϑ, Fig. 22 c) [66, 67].

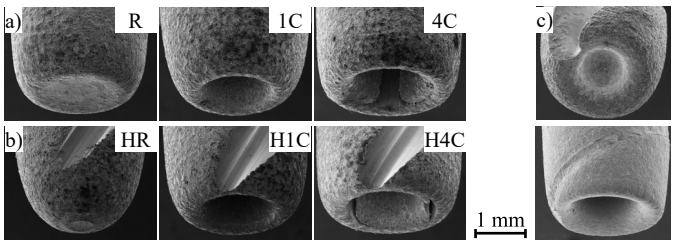

Fig. 22. SEM images of tool electrode tips; (a) without exterior flushing; (b) with exterior flushing; (c) flutes, clogged with electrode material.

Machining results using the six types of tool electrodes depicted in Fig. 23 and Table 3 show the complex correlations between the target parameters as well as the impossibility to improve them all together.

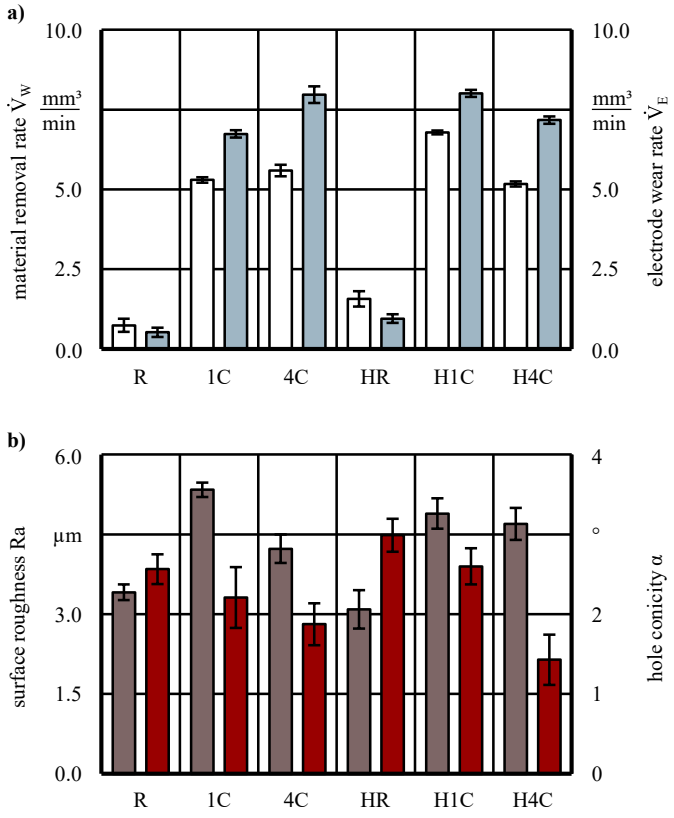

EDM machine tool:
AGIE compact 1, GF
MACHINING SOLUTIONS, Switzerland
Tool electrodes:
Brass, Table 2
Electrode diameter d_{el} = 3.00 mm
Flute angle α_f = 60.00 °
Flute depth d_f = 0.50 mm
Processing parameters:
Open circuit voltage $\hat{u}_i$ = 180.00 V
Discharge capacity C_e = 1.32 µF
Charge current i_C = 4.00 A
Ontime t_{on} = 18.00 µs
Offtime t_{off} = 2.40 µs
Compression = 40.00
Gain = 15.00

Workpiece electrode:
Elmax Superclean
(X170CrVMo18-3-1)
Machining depth d_m = 15 mm
Flushing parameters:
Rotational speed n = 400 1/min
Flushing pressure p_f = 2 MPa
Dielectric Fluid:
IME 63, OELHELD GMBH, Germany

□ Material removal rate $\dot{V}_W$
□ Electrode wear rate $\dot{V}_E$
□ Surface roughness Ra
□ Hole conicity α

Fig. 23. Experimental results for six types of tool electrodes with internal and external geometries; (a) MRR and EWR; (b) surface roughness Ra and hole conicity α.

The influence of the exterior flushing channel with respect to the MRR and EWR is most obvious for the comparison of rod types R and HR. The vastly increased values of MRR and EWR when using single- and four-channel tool electrodes instead, result from the application of pressure flushing and the direct evacuation of process residues.

Table 3 gives a very detailed quantitative overview over the influence of external and internal geometries on the target parameters visualized in Fig. 23, supplemented by the machining time t_{ero} and frontal area A_e.

Table 3. Comparison of process results with tool electrodes with internal and external geometries for improved flushing conditions.

Comparison	A_e	t_{ero}	MRR	EWR	Ra	α	Assumed reasons
R → 1C	↓ 18.2	↓ 91.0	↑ 612.2	↑ 1,426.6	↑ 56.4	↓ 13.8	I, VI
R → 4C	↓ 12.6	↓ 90.5	↑ 652.3	↑ 1,704.5	↑ 24.0	↓ 26.9	I, V, VI
HR → H1C	↓ 19.6	↓ 80.1	↑ 331.2	↑ 934.7	↑ 58.2	↓ 12.8	I, II, VI
HR → H4C	↓ 13.6	↓ 71.3	↑ 228.7	↑ 826.6	↑ 52.0	↓ 52.0	I, II, V, VI
R → HR	↓ 7.1	↓ 63.8	↑ 111.6	↑ 75.3	↓ 9.4	↑ 16.2	III, V
1C → H1C	↓ 8.7	↓ 20.0	↑ 28.1	↑ 18.8	↓ 8.4	↑ 17.6	II
4C → H4C	↓ 8.1	↑ 9.4	↓ 7.6	↓ 10.0	↑ 11.0	↓ 23.8	II, IV
1C → 4C	↑ 6.8	↑ 5.8	↑ 5.6	↑ 18.2	↓ 20.8	↓ 15.1	IV, V
H1C → H4C	↑ 7.4	↑ 44.7	↓ 23.8	↓ 10.4	↓ 4.0	↓ 45.0	IV, V

I Removal of debris by pressure flushing
II Additional space for debris and gas bubbles
III Removal of debris and gas bubble through exterior flushing channel
IV Change of frontal area A_e and flushing cross-section A_f
V Turbulences or radial velocity components $|c_{rad}|$
VI Improved cooling of the discharge zones

Legend:
↑ Increase
↓ Decrease
↕ Improvement
↕ Deterioration
All values in %.

Interactions of pressure flushing on the one hand and exterior flushing channels on the other hand call for a detailed analysis of the complex fluid flow within the working gap, using numerical methods and experimental measurements, i.e. with a high-speed camera. Fig. 24 visualizes the flushing conditions as a result of CFD simulations in the form of contour-plots and streamlines.

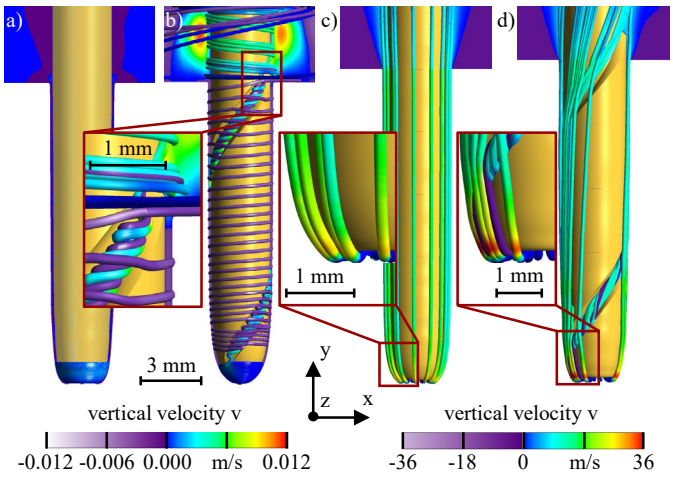

Tool electrode:
a) Rod (R)
b) Helix rod (HR)
c) Single-channel (1C)
d) Helix single-channel (H1C)

Main parameters:
Rotational speed n = 400 1/min
Flushing pressure p_f = 2 MPa

Fig. 24. Contour-plots and streamlines with regard to the vertical velocity v for the tool electrode types; (a) R; (b) HR; (c) 1C; (d) H1C.

Using pressure flushing, the dielectric is directly and straight flushed out of the bore hole with high vertical velocities of v ≥ 10 m/s. Vertical orientations of the related streamlines

prove the dominance of the flushing pressure p_f over the rotational speed n, Fig. 24 c) and d). For the H1C type, streamlines are not as evenly distributed as with the 1C type and show radial deflections. As with the HR type, there are streamlines following the circumferential flute, but they seem to be pulled out of the flute near the hole outlet and are, in addition, significantly less twisted. This insight is further emphasized by the observation that the lateral surfaces of the tool electrodes of type H1C exhibit asymmetrical distributions of discharge craters, which obviously result from this flow pattern, characterized by the deflected streamlines in Fig. 24 d). The band of discharge craters that has developed noticeably winds radially and exactly parallel to the flute of the tool electrodes, indicating an increased effective pulse frequency f_e in this region. This supports the conclusion that each combination of flute angle α_f and flute depth d_f is related to an optimal combination of the fluid mechanic parameters flushing pressure p_f and rotational speed n. These have to be set in a way that the ratio of the vertical velocity v to the radial velocity $c_{rad} = u + w$ decreases, and gas bubbles and debris are pulled into the flutes while being evacuated upwards.

A detailed signal analysis of the discharge current i_e and discharge voltage u_e by detecting rising and falling flanks allows for explanations and further quantification of the influence of internal and external flushing geometries on the process stability s_p and its target parameters, Fig. 25 [68]. For this purpose, frequency ratios λ are calculated as a ratio of the frequency of a respective type of discharge event with the pulse frequency t_p. Fully charging of the capacitor unfavorably covers four pulse cycle times t_p which increases the open-circuit frequency ratio λ_{op}.

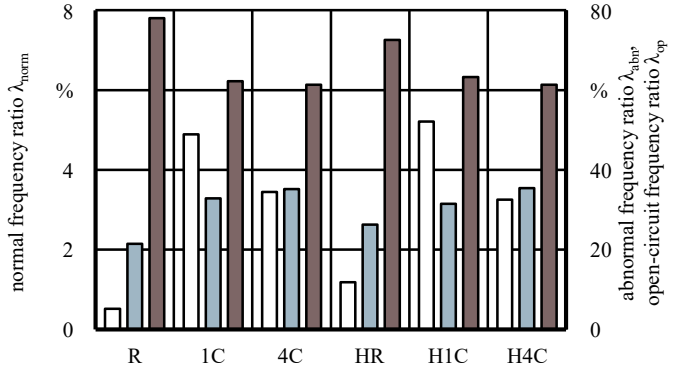

Measuring devices:
Voltage probe TT-HV 150,
TESTEC ELEKTRONIK GMBH, Germany
Current probe with amplifier
TCP303 with TCPA300,
TEKTRONIX INC., USA
Picoscope 3405D,
PICO TECHNOLOGY LIMITED, UK

Measuring range:
Intervall of the sinking depth
$12 \text{ mm} \leq d_s \leq 15 \text{ mm}$
Measuring parameter:
Sampling frequency $f_S = 1$ MHz
Normal frequency ratio λ_{norm}
Abnormal frequency ratio λ_{abn}
Open-circuit frequency ratio λ_{op}

Fig. 25. Signal analysis results for tool electrodes with internal and external geometries.

The following conclusions can be drawn:

- the normal frequency ratio λ_{norm} correlates with the MRR and the surface roughness Ra as well as with the use of inner flushing and the effective flushing cross-section A_f;
- the abnormal frequency ratio λ_{abn} drives the EWR, supplemental to the high energetic normal discharges; it is favored by turbulences or components of the radial velocity c_{rad} inside the working gap, both being induced by multi-channel tool electrodes and exterior flushing channels;
- the open-circuit frequency ratio λ_{op} correlates with the hole conicity α and is reduced by a decreased frontal area A_e and an increased flushing cross-section A_f.

Flushing conditions as well as the process stability s_p are perceptibly improved by providing additional space in the form of exterior flushing channels. Further investigations focus on illuminating the potential of tailored fluid mechanic parameter combinations for specific types of tool electrodes with exterior flushing channels as well as high-speed camera observations of the complex fluid flow within the working gap.

2.2.3. Validation of different tungsten carbide-cobalt grades as tool electrode material for EDM

Besides using brass, as in the previous section, tungsten carbide-cobalt (WC-Co) is a major tool electrode material in drilling EDM because of its thermophysical properties [4, 69]. Due to its limited machinability in cutting operations, conventional WC-Co materials have not been applied nor extensively analyzed for the application as tool electrode material in sinking EDM in the past [70].

The so far unknown correlations between material characteristics of WC-Co materials and corresponding process results shall be described by analyzing the process behavior of different WC-Co grades as tool electrode materials in sinking EDM [70]. The applied tool electrode materials were 17 different industrial relevant WC-Co grades from SUMITOMO GROUP, Japan, and GÜHRING KG, Germany. X-ray fluorescence spectroscopy revealed cobalt contents between $0.9\ \% \leq c_{co} \leq 17.0\ \%$ for the respective WC-Co grades, where the lowest measured cobalt content of $c_{co} = 0.9\ \%$ refers to the material without any binder phase. The respective grain sizes of $0.16\ \mu\text{m} \leq d_g \leq 0.76\ \mu\text{m}$ are related to the measured mean chord length $l_{c,mean}$ of the WC grains.

Processing results for the machining of Elmax Superclean (X170CrVMo18-3-1) regarding MRR and relative tool wear ϑ with 17 WC-Co grades are shown in Fig. 26. Cobalt content c_{co} is presented on the X-axis, whereas the grain size d_g, classified in four groups, is represented by the different graphs. The tendency of the relative tool wear ϑ to decrease with higher cobalt content c_{co} is clearly visible in Fig. 26 a). The outlier at the very left refers to the WC grade without any binder phase and should be considered separately from the other WC-Co grades. The decrease of the relative tool wear ϑ with increasing cobalt content c_{co} might be a consequence of the material characteristics of cobalt with its higher specific heat capacity c_p and slightly higher thermal conductivity λ compared to WC [71]. Consequently, a lower temperature increase $\Delta\vartheta_m$ occurs on the tool electrode surface, resulting in a reduced relative tool wear ϑ.

Another beneficial material characteristic of cobalt can be found concerning the electrical conductivity being $\kappa_{co} \approx 170$ kS/cm, which is more than three times higher compared to the electrical conductivity of WC with $\kappa_{WC} \approx 50$ kS/cm. The melting temperature of cobalt contradicts the presented results, with $T_{m,co} = 1{,}768$ K being much lower than $T_{m,WC} = 3{,}080$ K for WC. Nevertheless, the cobalt binder

phase, being the less stable component in this composite, leads to increased relative tool wear ϑ when reaching a critical cobalt content c_{co}. This can be seen for WC-Co grades with a grain size of $0.30\ \mu m \leq d_g \leq 0.45\ \mu m$, where an increase of the relative tool wear ϑ can be identified for the two WC-Co grades with cobalt content $c_{co} > 13$ %.

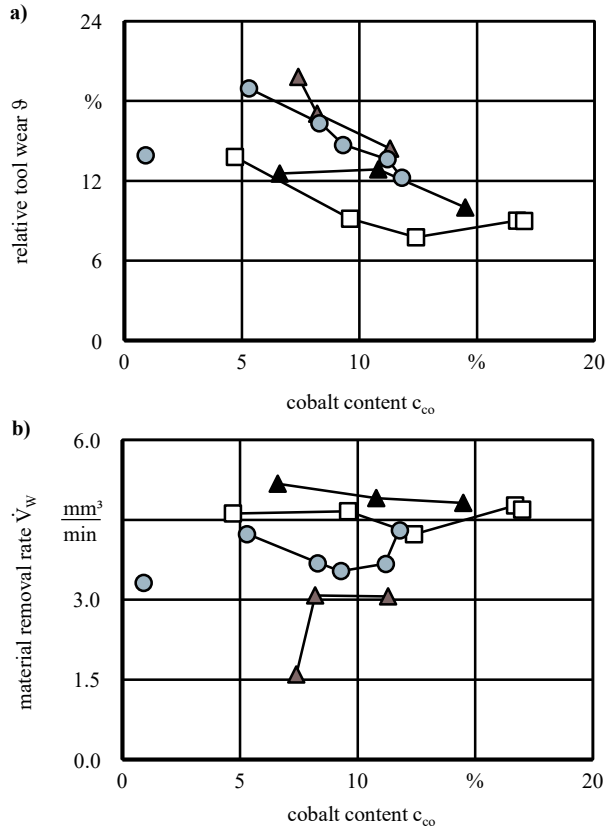

EDM machine tool:
Genius 1000 The Cube,
ZIMMER & KREIM, Germany
Processing parameters:

Sinking depth	d_s =	1.0 mm
Discharge current	i_e =	6.7 A
Discharge duration	t_e =	40.0 µs
Pulse interval time	t_0 =	20.0 µs
Open circuit voltage	$\hat{u}_i$ =	280.0 V

Workpiece electrode:
Elmax Superclean
Tool electrodes:
Tungsten carbide-cobalt
Cylindric samples
Electrode diameter d_e = 10.00 mm
▲ d_g > 0.60 µm
□ 0.30 µm ≤ d_g ≤ 0.45 µm
○ 0.20 µm ≤ d_g ≤ 0.25 µm
▲ d_g < 0.20 µm

Fig. 26. Comparison of process results using WC-Co with different grain sizes d_g; (a) relative tool wear ϑ; (b) MRR.

The MRR on the other hand shows no dependency on the cobalt content c_{co}, Fig. 26 b). In contrast, a higher grain size d_g is related to a higher MRR.

Similar relations have been identified for graphite tool electrodes in different studies [33, 72]. The grain size d_g influences the electrical conductivity κ or specific electrical resistivity ρ_R respectively, and consequently the amount of electric energy E_{el} that gets lost in the tool electrode material [33, 73].

Based on these results, one specific WC grade has been chosen to further analyse processing parameters in micro-EDM. The best set of parameters is compared to copper and graphite tool electrodes, both show much higher MRR compared to WC-Co tool electrodes, Fig. 27. In contrast, the relative tool wear for WC-Co tool electrodes reaches $\vartheta_{WC\text{-}Co} = 5.3$ %, unlike graphite with $\vartheta_{graphite} = 10.6$ % and copper with $\vartheta_{copper} = 14.6$ %. This reduction of the relative tool wear ϑ demonstrates a potentially beneficial application of WC-Co as tool electrode material in micro-EDM.

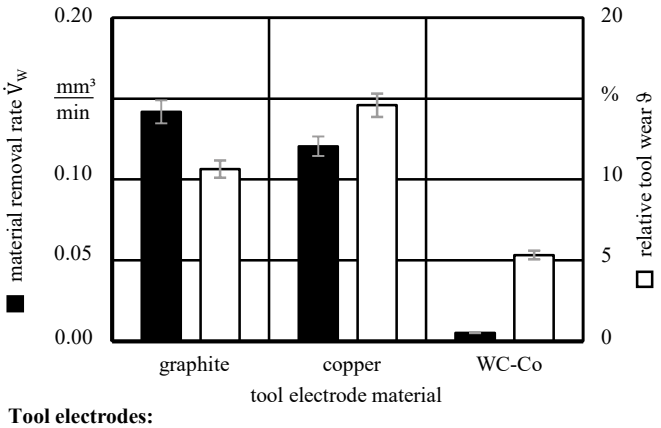

Tool electrodes:
Graphite EDM-3, POCO GRAPHITE INC., USA
Electrolytic copper E-Cu58
Tungsten carbide-cobalt WC-Co
Double bar samples
Frontal area A_e = 0.7 mm²
Processing parameters:
Sinking depth d_s = 0.3 mm
Discharge current i_e = 4.0 A
Discharge duration t_e = 11.0 µs
Pulse interval time t_0 = 32.0 µs
Open circuit voltage $\hat{u}_i$ = 65.0 V
Feed voltage U_F = 28.0 V

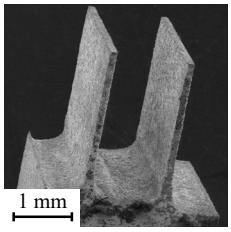

Tool electrode geometry

Fig. 27. Comparison of processing results between graphite, copper and WC-Co tool electrodes for micro-EDM.

2.2.4. WC tool electrodes with interior flushing channels made by additive manufacturing

Another investigation of applying WC-Co in the field of sinking EDM was realized by additive manufacturing (AM) of tool electrodes. For the machining of high aspect ratios φ, a flushing directly through the tool electrode, as commonly applied in drilling EDM, keeps being the best option for a reliable evacuation of debris and gas bubbles [74].

Application of pressure flushing in sinking EDM, for example through cylindrical internal flushing channels inside the tool electrodes, is being hindered due to increasing degrees of automation along modern process chains. Interior flushing channels highly increase the complexity of the tool electrode manufacturing. Consequently, this approach is hardly utilized. In most cases a flushing method of passive nature using electrode jumps has to be applied, despite having its limitations e.g. with high aspect ratio cavities.

As a result, AM has been identified as a suitable solution for tool electrode production and the implementation of interior flushing channels. AMORIM ET AL. [38] used a Mo-CuNi composite and identified that these tool electrodes showed better process results regarding MRR and relative tool wear ϑ than AM copper tool electrodes. Nevertheless, the results were inferior in comparison to solid copper tool electrodes. CZELUSNIAK ET AL. [39] analyzed the suitability of different materials for AM tool electrodes. Composite TiB_2-CuNi showed the best performance in the sinking EDM process, although the results were still inferior compared to solid copper tool electrodes. YANAGIDA ET AL. [41] investigated the use of AM copper tool electrodes whose heat treatment enabled

processing results similar to tool electrodes conventionally machined out of electrolytic copper. The additional use of interior flushing significantly enhanced high aspect ratio machining.

Especially the melting temperature ϑ_m of the tool electrode material has a great influence on the erosion strength c_m that can be used to classify tool electrode materials in terms of their wear resistance [4, 32]. Due to its thermophysical properties like a high melting temperature ϑ_m, a high specific heat capacity c_p and a high density ρ, tungsten carbide-cobalt (WC-Co) has an erosion strength c_m that is 6.4 or 5 times higher than the one of graphite or electrolytic copper respectively [70]. Due to this WC-Co is a suitable tool electrode material for dedicated EDM applications, see section 2.2.3 [75].

In order to investigate the EDM processing behavior of AM tool electrodes made of WC-Co, different sets of AM processing parameters were tested on the machine tool SLM250, SLM SOLUTIONS GROUP AG, Germany. It could be shown that the cobalt content c_{Co}, influenced by the AM processing parameters, possesses a significant influence on the MRR and relative tool wear ϑ. The post-processing technology hot isostatic pressing (HIP) was identified as another significant factor. HIP processed tool electrodes showed higher MRR and lower relative tool wear ϑ compared to the untreated tool electrodes [75]. This is confirmed by the findings of YANAGIDA ET AL. [41].

An EDM processing parameter analysis revealed a nearly perfect linear correlation between discharge current i_e and MRR, which is explained by the concomitant linear increase of the discharge energy W_e. In contrast to that, the relative tool wear ϑ and the surface roughness Ra showed a local minimum for a discharge current of $i_e = 10$ A.

By applying CFD simulations, different geometries and outlet positions for interior flushing channels in tool electrodes were investigated with the objective of identifying configurations which ensure a flow velocity c that is directed downstream in the whole working gap. Angled flushing channel outlets in the frontal area of the AM tool electrodes showed the best results in this context and consequently ensure a proper flushing in the working gap.

To contextualize the results of the AM tool electrodes regarding MRR and relative tool wear ϑ, these process results were compared to results of solid tool electrode materials made of graphite EX-75, IBIDEN K.K., Japan, and electrolytic copper E-Cu 58 as well as WC-Co CTS20, CERATIZIT GROUP, Luxembourg, Fig. 28.

The sinking depth was set to $d_s = 5$ mm and the applied processing parameters for sinking EDM were chosen as the given standard parameters for solid copper and graphite respectively, with a discharge current in the order of $i_e = 10$ A. This setting results in a surface roughness of Ra = 4.5 µm, corresponding to a class 33 according to VDI guideline 3400.

The MRR shows similar results for all tool electrode materials, except for the AM tool electrodes with interior flushing channels. This advantage leads to an increase of the MRR by more than 35 % to $\dot{V}_W = 4.2$ mm³/min and underlines the insufficiency of a passive flushing based on electrode jumps.

The relative tool wear ϑ in Fig. 28 b) mostly depicts better results for solid tool electrodes. Nevertheless, interior flushing reduces the relative tool wear by 34 % from $\vartheta = 5.9$ % to $\vartheta = 3.9$ % for AM WC-Co.

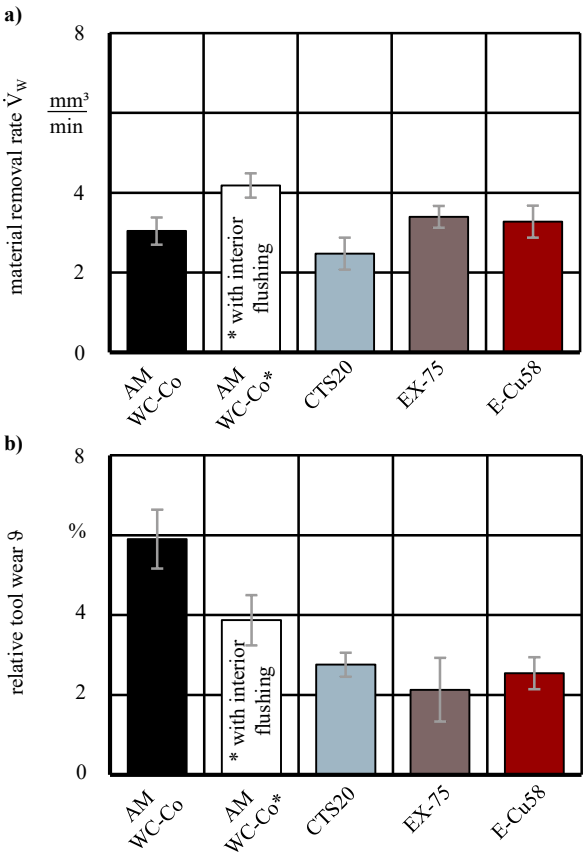

EDM machine tool:
Genius 1000 The Cube,
ZIMMER & KREIM GMBH & CO. KG, Germany
Processing parameters:
Discharge type: static impulse
Dielectric fluid:
IonoPlus IME-MH, OELHELD GMBH, Germany
Workpiece material:
ELMAX Superclean (X170CrVMo18-3-1)
Sinking depth: d_s = 5 mm

Tool electrodes:
Bar electrodes
Frontal area:
A_e = 1 mm x 10 mm
Tool electrode materials:
Additively manufactured WC-Co
Tungsten carbide CTS 20
Graphite EX-75
Electrolytic copper E-Cu58

Fig. 28. Comparison of different tool electrode materials regarding; (a) MRR; (b) relative tool wear ϑ.

The presented investigations show that an application of AM tool electrodes made of WC-Co enables improvements regarding MRR. Nevertheless, the relative tool wear ϑ stays at a higher level. Future investigations will include the application of dedicated AM technologies and machine tools for the production of tool electrodes for sinking EDM as well as additional studies of AM processing parameters in order to improve structural characteristics of AM parts. Post-processing like flow grinding, blasting and immersed tumbling will be investigated in order to improve the surface quality of AM tool electrodes.

2.2.5. Boron doped CVD-diamond as tool electrodes for micro-EDM

A promising approach to improve EDM process results, especially in micro-EDM, is the use of boron-doped chemical vapor deposition (CVD)-diamond as tool electrode material

[76]. The material is especially suited for this purpose due to its thermophysical properties, such as high melting temperature ϑ_m, high thermal conductivity λ and high mechanical strength σ at low mass m [71].

In a first set of trials, the influence of different processing parameters was validated. Only the discharge capacity C_e and open circuit voltage $\hat{u}_i$ showed significant effects on the MRR and relative tool wear ϑ for the applied relaxation pulses. Different workpiece materials have been machined with a sinking depth of $d_s = 0.5$ mm using tool electrodes with a frontal area of $A_e = 10$ mm × 0.04 mm and an electrode length of $l_{el} = 5$ mm. This high aspect ratio of $\varphi = 12.5$ facilitated the identifiability of effects on processing and wear behavior. In Fig. 29, process results for varied discharge capacities C_e and open circuit voltages $\hat{u}_i$ are visualized.

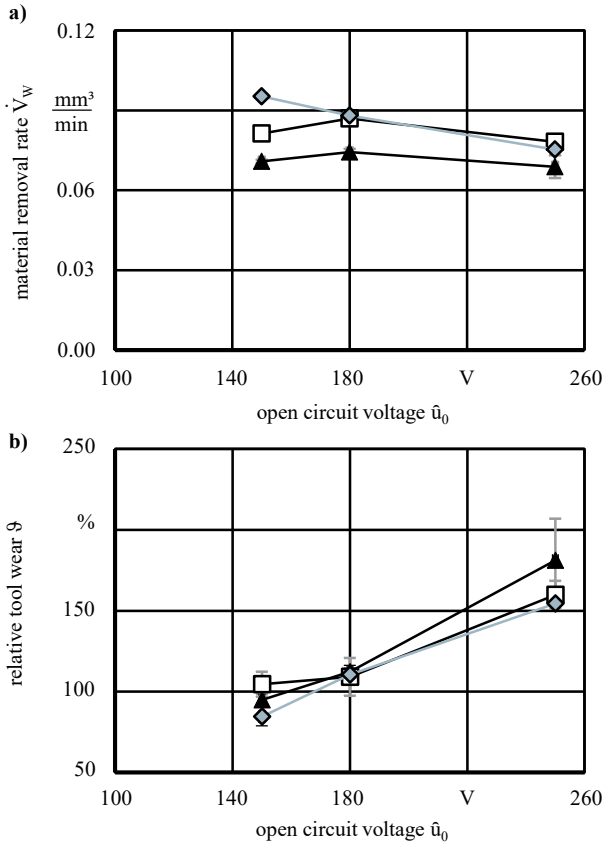

EDM machine tool:
AGIE compact 1, GF MACHINING SOLUTIONS, Switzerland
Processing parameters:
Ontime t_{on} = 10.0 µs
Offtime t_{off} = 10.0 µs
Compression = 10.0
Gain = 30.0
Tool electrode:
Boron doped CVD-diamond
Sinking depth d_s = 0.50 mm
Workpiece electrode:
Cold-work steel 90MnCrV8
Dielectric fluid:
IME 63, OELHELD GMBH, Germany
▲ Discharge capacity C_e = 5.70 nF
□ Discharge capacity C_e = 6.90 nF
◇ Discharge capacity C_e = 8.43 nF

Fig. 29. Process results for sinking EDM with boron doped CVD-diamond tool electrodes regarding; (a) material removal rate $\dot{V}_W$; (b) relative tool wear ϑ.

The MRR in Fig. 29 a) decreases slightly with increased open circuit voltage $\hat{u}_i$ when applying the highest discharge capacity of $C_e = 8.43$ nF. For discharge capacities of $C_e = 6.9$ nF and $C_e = 5.7$ nF, the open circuit voltage $\hat{u}_i$ hardly influences the MRR. The higher discharge energies W_e caused by an increasing open circuit voltage $\hat{u}_i$ lead to amplified discharge currents i_e and finally to an increased relative tool wear ϑ, illustrated in Fig. 29 b). This effect results in a decreased MRR for high open circuit voltages $\hat{u}_i$, although the machining times t_{ero} were reduced. The best combination of MRR and relative tool wear ϑ was achieved by applying a discharge capacity of $C_e = 8.43$ nF and an open circuit voltage of $\hat{u}_i = 150$ V.

With the objective of an efficient replication of micro-structures, the initial machining of these micro-structures into the boron doped CVD-diamond tool electrode was realized indirectly by preparing a copper substrate for the CVD-process using micro-milling. Within the CVD-process, boron is included to enable electrical conductivity κ, and the micro-structures are indirectly transferred via layer-by-layer deposition of the boron doped CVD-diamond. The separation of the copper substrate and the boron doped CVD-diamond marks the final step. In addition to this procedure, direct structuring of a plainly deposited boron doped CVD-diamond layer has been realized by laser ablation. The indirect structuring is shown in Fig. 30.

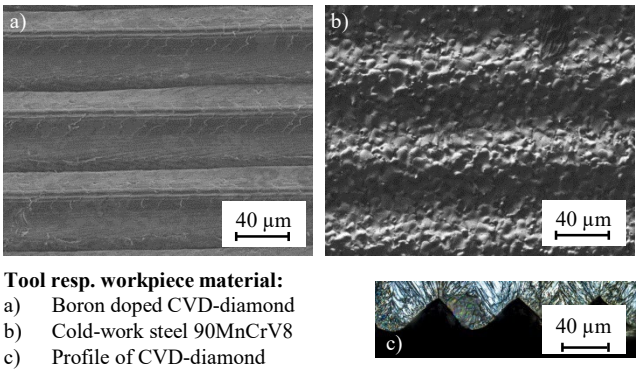

Tool resp. workpiece material:
a) Boron doped CVD-diamond
b) Cold-work steel 90MnCrV8
c) Profile of CVD-diamond
Applied machining system:
a) Primacon PFM 4024-5D/HF & CVD system CC800/Dia-5 Katharina
b) AGIE Compact 1
Measurement system:
a) b) Nikon JC-5000 SEM
c) Leica DM6000M

Fig. 30. Application of indirectly structured boron doped CVD-diamond tool electrodes.

Application of micro-structured boron doped CVD-diamond as tool electrode for micro-EDM processing is feasible. Applying the boron doped CVD-diamond foils, the micro-structures could be machined in cold-work steel 90MnCrV8 as well as WC-Co K40F by micro-EDM. Machining the ceramic SiSiC with boron doped CVD-diamond on the other hand was not possible using micro-EDM due to the high discharge energies W_e that are required for sufficiently evaporating or removing the material respectively. In view of the very time-consuming CVD-process, boron doped CVD-diamond tools are very cost intensive. Nevertheless, boron doped CVD-diamond proved to be highly wear-resistant and enabled stable machining conditions in micro-EDM experiments.

In experiments with static pulses, machining without almost any wear was achieved for aspect ratios $\varphi \leq 10$ in cold-work steel 90MnCrV8. Higher aspect ratios φ are possible, but also associated with very long machining times t_{ero}. Due to discharge durations of these static pulses in the order of

$t_e = 10$ µs, which are accompanied with increased discharge energies W_e, this zero-wear technology for boron doped CVD-diamond tool electrodes did not stand out as being suitable for micro-EDM.

2.2.6. Oxidized tool electrodes for drilling EDM

Flushing methods like inverted pressure flushing or exterior flushing channels seek to use low pressure to pull debris and gas bubbles out of the lateral working gap during drilling EDM, see sections 2.1.3 and 2.2.2. AM tool electrodes and actuated tool electrode segments additionally enable flushing methods of active nature for sinking EDM due to the application of interior flushing channels or the generation of transverse waves, see sections 2.2.4 and 2.2.1. Active redistribution of discharges allows the ascend of debris and gas bubbles during periods in which selected tool electrode segments are switched off, see section 2.1.5.

Acknowledging the presence of debris and gas bubbles in the lateral working gap still allows to reduce the negative effects, causing process instabilities, a decreased MRR or an increased hole conicity α. Another promising approach to overcome state-of-the-art limitations in EDM is given by a dedicated oxidation of the tool electrode surface [77, 78, 79]. Formation of an oxidation layer on the tool electrode's surface supposably results in an increase of the specific electrical resistivity ρ_R at the tool electrode surface. As a consequence, the potential of contaminations to bridge the lateral working gap and to negatively influence the process stability s_p through abnormal discharges in the form of arcing and short-circuiting is significantly reduced.

To analyze these effects, oxidation of copper tool electrodes was investigated in an air atmosphere for oxidation temperatures of $\vartheta_{oxi} = 200$ °C and $\vartheta_{oxi} = 250$ °C, applying different oxidation times $10 \text{ min} \leq t_{oxi} \leq 35$ min. Treated tool electrodes were subsequently analyzed concerning color and oxide layer thickness d_{oxi} and finally used to machine through holes by drilling EDM. Surfaces of the oxidized tool electrodes are depicted in Fig. 31.

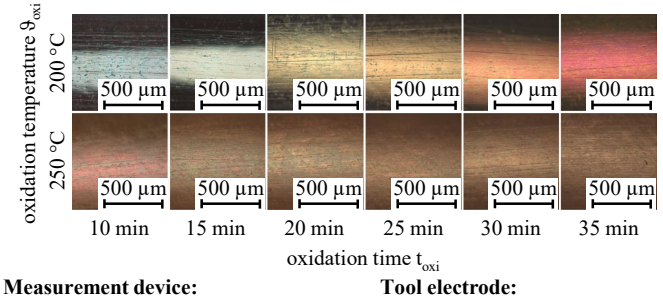

Measurement device:
Optical microscope Axioskop 50
Magnification M = 50

Tool electrode:
Copper
Electrode diameter $d_{el} = 2$ mm

Fig. 31. Surface images of oxidized tool electrodes in dependence of the oxidation time t_{oxi} and oxidation temperature ϑ_{oxi}.

Following its phase diagram, the first oxidation stage Cu_2O is formed, when copper is exposed to thermal energy under atmospheric conditions. Cu_2O appears to be red under crossed Nicols and is stable up to oxidation temperatures of $\vartheta_{oxi} = 250$ °C [80]. Above that, the second oxidation stage CuO is formed, being black in color. At the applied oxidation temperature of $\vartheta_{oxi} = 200$ °C, the oxide layer thickness d_{oxi} of Cu_2O grows with increasing oxidation time t_{oxi}, explaining the stepwise change of the surface color from yellow to red hue. The gray-blue color for oxidation times $t_{oxi} < 15$ min origins from an oxygen-rich blue skin, the thickness of which determines the hue and intensity of the color [80].

On the contrary, after treatment with an oxidation temperature of $\vartheta_{oxi} = 250$ °C, where Cu_2O as well as CuO are both present, hardly any difference in the oxidized surface can be identified [81]. At an oxidation time of $t_{oxi} = 10$ min the red Cu_2O still dominates over the black CuO, which prevails for increasing oxidation times $t_{oxi} > 10$ min due to superposition and transformation, resulting in a brown color of cumulative darkness instead. According to VALLADARES ET AL. [81], both oxides have a higher specific electrical resistivity ρ_R than electrolytic copper. However, a 4-point measurement revealed, that the specific electrical resistivity of tool electrodes made of electrolytic copper, at $\rho_R = 0.23$ Ω mm²/m, decreased by up to 14 % as a consequence of the treatment with an oxidation temperature of $\vartheta_{oxi} = 200$ °C and by up to 16 % using an oxidation temperature of $\vartheta_{oxi} = 250$ °C. This indicates, that not only the pure oxide layer, but also the copper base material was exposed to electrical contact and therefore measured. Consequently, the copper base material was changed by other means, for instance by crystal recoveries caused by heat treatment. In this process, crystal defects such as vacancies or dislocations are eliminated or mended, resulting in a decrease in specific electrical resistivity ρ_R and, at the same time, a slight decrease in initial hardness according to VICKERS of HV = 120 HV0.1. For an oxidation temperature of $\vartheta_{oxi} = 200$ °C the hardness according to VICKERS was decreased by 7 % and for $\vartheta_{oxi} = 250$ °C by 8 % respectively.

In addition to surface images, cross-sectional SEM images are shown in Fig. 32 to determine the oxide layer thickness d_{oxi}. Possible changes in the micro-structure due to recrystallization can be ruled out, because the oxidation temperatures used are below the necessary $\vartheta_{oxi} = 500$ °C.

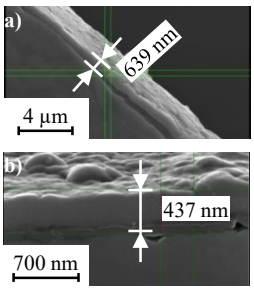

Measurement device:
SEM DSM 982 Gemini
CARL ZEISS AG, Germany
Magnification a) M = 7,000
b) M = 50,000
Acceleration voltage a) U_A = 20,000 V
b) U_A = 15,000 V

Tool electrode:
Copper
Electrode diameter $d_{el} = 2$ mm

Fig. 32. Cross-sectional SEM images of oxidized tool electrodes with an oxidation time of $t_{oxi} = 35$ min and an oxidation temperature of (a) $\vartheta_{oxi} = 250$ °C and (b) $\vartheta_{oxi} = 200$ °C.

Measurements of the oxide layer thickness d_{oxi} are presented in Fig. 33. As expected, increasing oxidation temperatures ϑ_{oxi} and oxidation times t_{oxi} enlarge the oxide layer thickness d_{oxi}. Consequently, the highest oxide layer thickness of $d_{oxi} = 640$ nm was measured by an oxidation temperature of $\vartheta_{oxi} = 250$ °C and an oxidation time of $t_{oxi} = 35$ min. For the lower oxidation temperature of $\vartheta_{oxi} = 200$ °C and an oxidation time of $t_{oxi} = 10$ min the oxide layer thickness d_{oxi} was too low to be measured, which is why the lowest oxide layer thickness of $d_{oxi} = 466$ nm resulted from an oxidation time of $t_{oxi} = 25$ min.

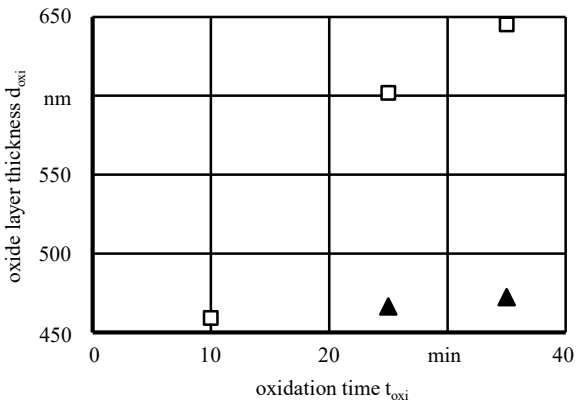

Tool electrode:
Copper
Electrode diameter d_{el} = 2 mm
Oxidation temperature ▲ ϑ_{oxi} = 200 °C
□ ϑ_{oxi} = 250 °C

Fig. 33. Oxide layer thickness d_{oxi} in dependence of the oxidation time t_{oxi} and oxidation temperature ϑ_{oxi}.

Using tool electrodes prepared by this procedure, drilling EDM experiments were carried out to machine through holes in the steel Elmax Superclean (X170CrVMo18-3-1) with an aspect ratio of $\varphi = 4.5$. A flushing strategy of passive nature using electrode jumps was applied. Results in terms of MRR as well as the linear wear of the tool electrode Δl_E are related to results of reference tool electrodes made of pure copper, Fig 34.

For tool electrodes treated at oxidation temperatures of $\vartheta_{oxi} = 200$ °C, no trend concerning the MRR can be stated for increasing oxidation times t_{oxi}. The comparison with Fig. 33 suggests that a critical oxide layer thickness $d_{oxi} = 500$ nm for a sufficient increase of the specific electrical resistivity ρ_R of the tool electrode's surface was not achieved for an oxidation temperature of $\vartheta_{oxi} = 200$ °C and oxidation times of $t_{oxi} = 20$ min and $t_{oxi} = 30$ min as well as an oxidation temperature of $\vartheta_{oxi} = 250$ °C and an oxidation time of $t_{oxi} = 10$ min. These MRR values were even 25 % below the MRR of the reference tool electrode with $\dot{V}_W = 0.31$ mm³/min. High standard deviations σ imply reduced process stabilities s_p and result from a combination of the absence of rotation and pressure flushing, which lead to temporal accumulations of debris, as well as related difficulties during workpiece breakthrough and the necessity for a critical oxide layer thickness d_{oxi} mentioned above.

In contrast, oxidation temperatures of $\vartheta_{oxi} = 250$ °C generally result in an increased MRR compared to the reference tool electrodes. An increase of the oxidation time t_{oxi} leads to a steady rise of the MRR. Although crystal recoveries entail an increased electrical conductivity κ in the copper base material for both oxidation temperatures ϑ_{oxi} and therefore generally benefit the ED process, the effect of oxide layer thicknesses of $d_{oxi} > 500$ nm to reduce the probability of discharge events in the lateral working gap is much more significant to the target parameters, Fig. 34. Accordingly, the highest MRR, which at $\dot{V}_{W,max} = 1.57$ mm³/min is five times higher than the MRR of the reference tool electrode, could be achieved for the maximum values of the oxidation temperature ϑ_{oxi} and the oxidation time t_{oxi}, representing the most beneficial combination in terms of an increased electrical conductivity κ due to crystal recovery and the prevention of discharge events in the lateral working gap due to the highest value for the oxide layer thickness d_{oxi}.

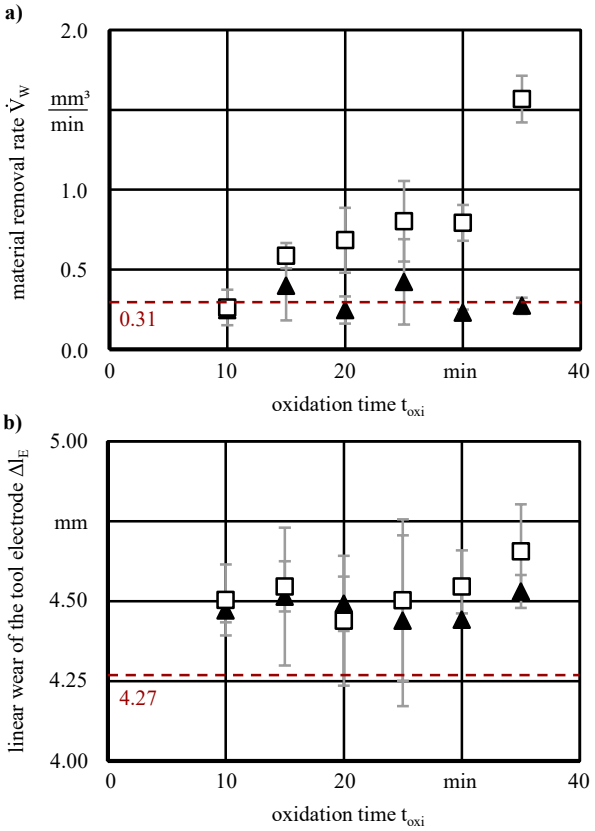

EDM machine tool:
AGIE compact 1,
GF MACHINING SOLUTIONS, Switzerland
Processing parameters:
Open circuit voltage $\hat{u}_i$ = 160.0 V
Discharge capacity C_e = 1.0 µF
Charge current i_C = 5.6 A
Ontime t_{on} = 32.0 µs
Offtime t_{off} = 18.0 µs
Dielectric fluid:
IME 63, OELHELD GMBH, Germany

Flushing parameters:
Electrode jumps
Lifting interval t_l = 30 s
Workpiece electrode:
Elmax Superclean
(X170CrVMo18-3-1)
Machining depth d_m = 9 mm
Tool electrode:
Copper
Electrode diameter d_{el} = 2 mm
Oxidation temperature ▲ ϑ_{oxi} = 200 °C
□ ϑ_{oxi} = 250 °C
Reference

Fig. 34. MRR and linear wear of the tool electrode Δl_E in dependence of the oxidation time t_{oxi} and oxidation temperature ϑ_{oxi}.

However, the linear wear of the tool electrode Δl_E universally tends to be increased by higher oxidation temperatures ϑ_{oxi} and oxidation times t_{oxi}. Likewise, the highest linear wear of the tool electrode $\Delta l_{E,max}$ using oxidized tool electrodes was observed for the highest values of the oxidation temperature ϑ_{oxi} and the oxidation time t_{oxi}, as it exceeded the reference value of $\Delta l_E = 4.27$ mm by 8 %.

As a result, higher oxidation temperatures ϑ_{oxi} and oxidation times t_{oxi} led to a higher oxide layer thickness d_{oxi} of the tool electrodes, which resulted in an increased MRR due to a presumable concentration of discharge events in the frontal working gap and resulting higher process stabilities s_p. The detailed influence of the heat treatment of tool electrodes on the drilling EDM process will be a subject of future investigations. Composition of the oxide layer for instance may be a critical factor, because both Cu_2O and CuO can be formed in the temperature range that drives the oxidation. The exact composition of the oxide layer and the dependencies on the

oxide layer depth d_t that grows into the base material as well as the resulting effects on the drilling EDM performance will be analyzed in the future.

2.2.7. Carbon fiber tool electrodes

Academic approaches from the penultimate decade enable micro- and sub-micro ED drilling of boreholes with hole diameters of $d_h = 2.9$ µm in stainless steel X5CrNi18-10 (1.4301), using a specially prepared tungsten carbide tool electrode with an electrode diameter of $d_{el} = 1.8$ µm on a Nano EDM AE 05 machine tool from SODICK CO., LTD., Japan [82]. Even hole diameters of $d_h < 1$ µm in brass or zinc with aspect ratios $\varphi < 3$ are possible with EDM, using tungsten or silicon tool electrodes with electrode diameters of $d_{el} = 0.4$ µm or $d_{el} = 0.15$ µm respectively and applying ultrasonic oscillation [83]. Nevertheless, major challenges for micro-ED drilling with hole diameters $d_h \leq 0.1$ mm still persist. Production, handling and positioning of pre-processed tool electrodes is most challenging, because required tool electrodes have to be manufactured in an additional process step by use of wire-electrical discharge grinding (WEDG) or electrochemical machining (ECM) [83, 84, 85]. The high electrode wear rate (EWR) $\dot{V}_E$ limits the tool life of tool electrodes of that order, because tool electrodes will not be available indefinitely and the hole depth h_d is limited by the restricted flushing possibilities [36, 85, 86, 87].

Electrode diameters 5 µm $\leq d_{el} \leq$ 10 µm of carbon fibers, their mechanical properties as well as their high electrical conductivity $\kappa > 0.625$ kS/cm predestine the use of single carbon fibers as tool electrodes for micro-ED drilling [88]. TRYCH ET AL. [36, 37] did not succeed in applying single carbon fibers for a stable and reproducible micro-ED drilling of boreholes with hole diameters in the order of $d_h < 20$ µm. According to the authors, the EWR with 40 µm³/s $\leq \dot{V}_E \leq$ 100 µm³/s considerably excels the MRR. They also identified essential necessities of controlling the position of the tool electrode tip and preventing its sudden deflection to enable a controlled process and sufficient processing results.

With the objective to overcome these challenges and investigate manufacturing technologies and machining strategies for the machining of stainless steel X10CrNi18-8 (1.4310) UHLMANN ET AL. [88, 89] perform fundamental research on these topics. Based on an evaluation of the properties of single polyacrylonitrile (PAN) and mesophase-pitch (MP) carbon fibers, an analysis of the removal mechanisms and gas bubble formation resulting from single discharges is carried out. The development of a dedicated machine tool with adapted control architecture based on the presented machine tool for dry EDM in section 2.1.1 enables the elaboration of manufacturing technologies for large aspect ratios $\varphi \geq 10$.

Fig. 35 shows SEM images of four different types of carbon fibers that are part of ongoing research with the objective of enabling the utilization of carbon fibers for micro-ED drilling. Fig. 36 shows first drilling results without using a special handling system. Unlike previous works in this field, these results prove the great applicability of MP carbon fibers as tool electrode material for micro-ED drilling, but also indirectly confirm deflections of the fiber tip as a result of discharges, visible as enlarged hole inlets.

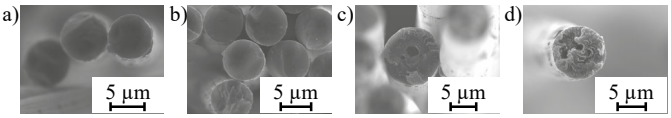

Fig. 35. SEM images of different types of carbon fibers; (a) PAN IMS65; (b) PAN HTS45; (c) MP YS-95A; (d) MP XN-90-60S.

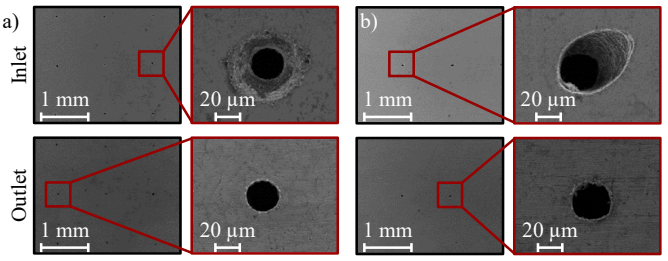

c) Workpiece height h	20 µm	50 µm
Material removal rate $\dot{V}_W$	9 µm³/min	8 µm³/min
Electrode wear rate $\dot{V}_E$	2 µm³/min	4 µm³/min
Hole diameter d_h	24 µm $\leq d_h \leq$ 26 µm	26 µm $\leq d_h \leq$ 30 µm

EDM machine tool:
Quadratron 1 with generator AT Spirit 2, GF MACHINING SOLUTIONS, Switzerland
Dielectric fluid:
IonoPlus IME-MH, OELHELD GMBH, Germany
Tool electrode:
MP-based carbon fibre XN-90-60S NIPPON GRAPHITE FIBER CORPORATION, Japan
Electrode diameter $d_e = 0.01$ mm
Workpiece electrode:
Stainless steel 1.4310

Fig. 36. Micro-holes machined with MP carbon fibers in two workpiece heights; (a) h = 20 µm; (b) h = 50 µm; (c) quantified results [89].

To meet the need for reproducible and accurate positioning, a special handling system for clamping, guidance, precise positioning as well as electrical contacting of carbon fiber tool electrodes with no preparation time has been developed, Fig. 37. The clamping jaw is coated with xylene and therefore allows to locally damp the clamping force F_C and to prevent damaging the fibers. The movable jaw establishes the electrical contact to the copper plate that is itself connected to the machine tool generator. A glass micro-pipette made of borosilicate glass 3.3 with an inner tip diameter 7 µm $\leq d_t \leq$ 13 µm works as a guidance to ensure accurate and repeatable positioning of the fibers. Besides the general difficulty of handling tool electrodes of this size, this handling system provides the basis for extensive experiments, because the carbon fibers can be easily removed, replaced and positioned. A low-pressure vacuum cup at the tip of the glass micro-pipette additionally eases the experimental setup.

A thermal treatment by pyrolysis of commercially available carbon fibres is necessary to improve their handling for the purpose of micro-ED drilling. Electrochemical treatment and additional sizing of the continuous carbon fiber filaments during their production and prior to winding them on bobbins aim at improving the adhesion to the matrix resin in which the filaments are usually further processed to carbon fiber-reinforced polymers. The objective of a pyrolysis previous to micro-ED drilling experiments is to remove this size, because it significantly hinders the separation of single carbon fibers out of the roving. Possible negative effects of the pyrolysis on the mechanical properties of the carbon fibers must consequently be considered and are part of future investigations.

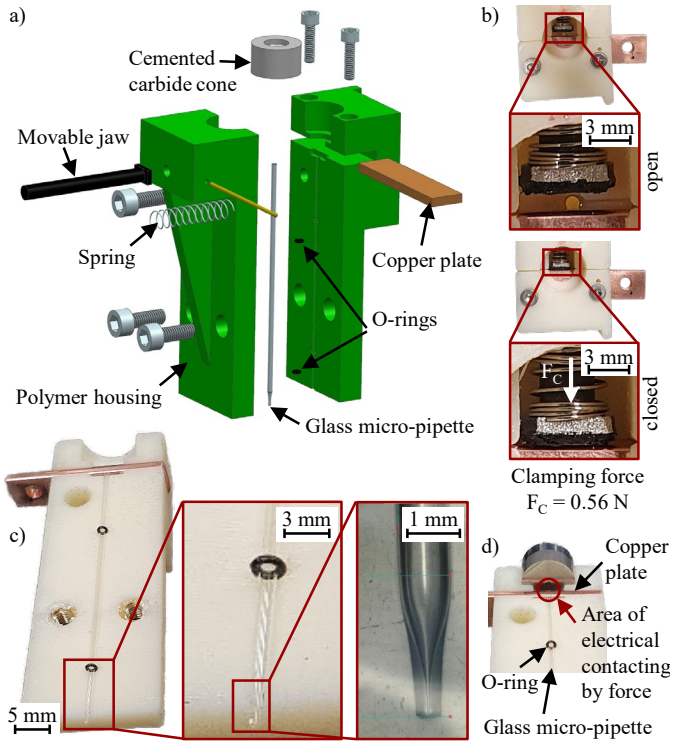

Fig. 37. Handling system for single carbon fibers as tool electrodes in micro-EDM; (a) exploded view of CAD; (b) clamping; (c) guidance; (d) electrical contacting [88].

2.3. Alternative dielectric fluids

Dielectric fluids have a significant influence on the material removal process. Therefore, selecting a suitable dielectric fluid with appropriate electrical, mechanical and thermal properties for a machining purpose is of great importance.

Beyond that, in recent years gaseous process media have been a focus of research. The consequences of a replacement of liquid dielectrics by gases are a reduction of the dynamic viscosity η, an increase of the velocity c of the fluid in the working gap when using pressure flushing, independence from the machine tank and possible machining in previously unrealizable positions. Therefore, the use of gaseous dielectrics for EDM promises advantages in terms of handling because the gases are not flammable and do not need deionization. An implementation of manufacturing technologies and machining strategies for dry-ED drilling of the high-performance ceramics Si_3N_4-TiN and TiB_2 as well as the metals 18CrNi8 (1.5920), Inconel 718 (2.4668) and PMHS 6-5-4 (1.3361) has been performed by SCHIMMELPFENNIG [47], YABROUDI [90] and UHLMANN ET AL. [20, 91]. For this purpose, an increased process understanding has been gained by analyzing removal mechanisms based on single discharge craters and debris particles, process enhancing pure gases as well as flushing conditions [47, 90, 91]. Experiments were carried out on a unit for drilling EDM Quadratron 1 with a generator of type AT Spirit 2 of the company GF MACHINING SOLUTIONS, Switzerland. Within these investigations roughing and finishing technologies for the industrial application of alternative dielectric fluids could be successfully derived [47].

Fig. 38 shows single discharge craters for different materials. These elucidate different material removal mechanisms of the high-performance ceramics Si_3N_4-TiN (silicon-nitride 45 % and titanium-nitride 55 %) and TiB_2 compared to metals.

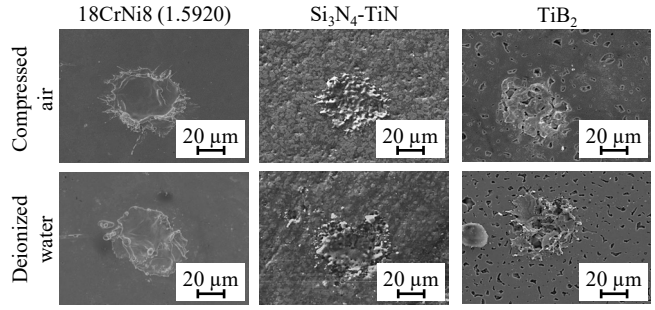

Tool electrode:
Cemented carbide
Electrode diameter d_{el} = 0.1 mm

Processing parameters:
Open circuit voltage $\hat{u}_i$ = 250.0 V
Discharge capacity C_e = 15.0 nF

Fig. 38. SEM images of single discharge craters, ignited under gaseous and liquid atmosphere [47].

In case of metals there is pure melting of the material, whereas the removal of TiB_2 is mainly based on spalling, the breaking of whole particles. As a composite, Si_3N_4-TiN exhibits process characteristics of both phenomena. As with metals, the formation of a molten layer can be observed, as well as higher MRR and larger lateral working gap widths s_l, compared to TiB_2.

The use of process enhancing gases with a high flushing pressure of $p_f \leq 8$ MPa allows to specifically develop and apply roughing and finishing technologies. Using tubular cemented carbide tool electrodes with an electrode diameter of d_{el} = 0.3 mm, finishing of Si_3N_4-TiN with a high contour accuracy and a relative linear wear $\vartheta_l < 1$ % is enabled by use of argon or nitrogen. For machining TiB_2 helium may be preferred for finishing over the other gases examined. These three gases share the characteristic of being inert or even noble gases, which prevents oxidation and decomposition effects on the tool and workpiece electrode. Consequently, this property makes them particularly suitable for finishing operations. For both ceramics, oxygen enables roughing with high process stability p_s and high values of the MRR, see Table 4 [47, 91].

Table 4. Comparison of MRR and EWR for drilling EDM of high-performance ceramics with pure gases, air and deionized water [47].

Si_3Ni_4-TiN	MRR in mm³/s	EWR in mm³/s	Application
Argon	0.00051	0.00040	Low-wear finishing
Oxygen	0.02844	0.58568	Roughing
Nitrogen	0.00060	0.00035	Low-wear finishing
Air	0.00731	0.03976	Reference
Water	0.01340	0.07069	Reference
TiB_2	MRR in mm³/s	EWR in mm³/s	Application
Helium	0.00063	0.01571	Low-wear finishing
Oxygen	0.00194	0.18102	Roughing
Air	0.00065	0.10780	Reference
Water	0.00085	0.00840	Reference

For dry-ED drilling of metals no positive influence of pure gases could be noted. Furthermore, the use of oxygen could not be controlled on the commercial machine tool. Finally, it has to be stated that electrode rotation is essential for the process stability p_s and the prevention of welding. Premature spark

breakdowns while maintaining actually capacitor-controlled plasma channels raise requests for a specialized generator technology. Reasons for premature spark breakdowns and special discharge phenomena can be found in the extremely small frontal working gaps $3.5\ \mu m \leq s_f \leq 6.0\ \mu m$ and the special breakdown behaviour in gases, see section 1 [17].

Rotating tubular tool electrodes made of cemented carbide with diameters of $0.1\ mm \leq d_{el} \leq 0.3\ mm$ were used for the machining of high-precision bores. Compressed air with flushing pressures of $p_f \leq 80$ bar was applied to the spindle for dry EDM, developed by IWF of the TU BERLIN (Fig. 4), and to a spindle focussing on the industrial application of dry-ED drilling by use of conventional EDM machine tools, developed in cooperation with HUGO RECKERTH GMBH, Germany, see Fig. 39. The rotational speed of the latter covers a range of $3{,}000\ 1/min \leq n \leq 20{,}000\ 1/min$.

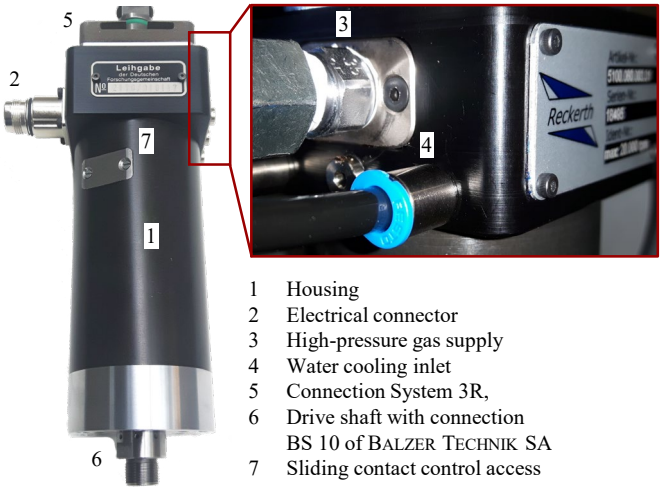

1 Housing
2 Electrical connector
3 High-pressure gas supply
4 Water cooling inlet
5 Connection System 3R,
6 Drive shaft with connection BS 10 of BALZER TECHNIK SA
7 Sliding contact control access

Fig. 39. Spindle for dry EDM, developed by IWF of the TU BERLIN with HUGO RECKERTH GMBH, Germany.

Fig. 40 shows exemplary machining results for dry-ED drilling in Si_3N_4-TiN, TiB_2, Inconel 718 and PMHS 6-5-4. These results support the notion that the removal mechanism of metals significantly differs from those of ceramic materials, mainly visible through a layer of reattached material around and inside the bore holes in metal workpieces. This layer can be completely eliminated by post-treatment in an ultrasonic bath, using diluted citric acid [21].

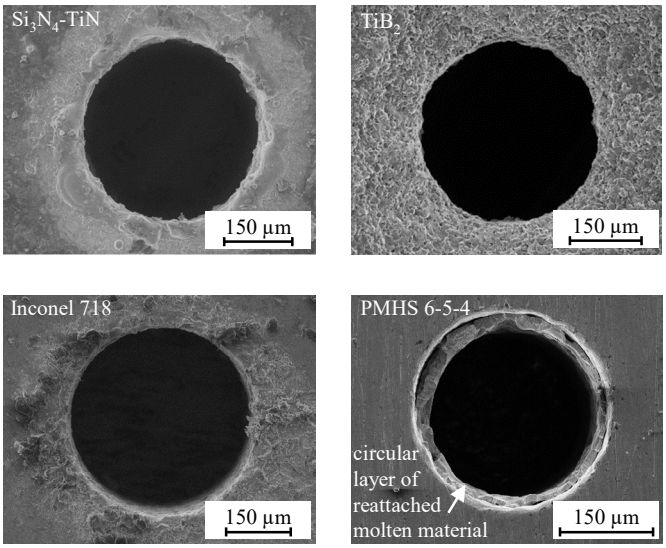

EDM machine tool:
Quadratron 1 with generator AT Spirit 2, GF MACHINING SOLUTIONS, Switzerland
Tool electrodes:
Cemented carbide
Electrode diameter d_{el} = 0.3 mm
Workpiece electrodes:
Workpiece height h = 1.0 mm
Dielectric fluid:
Compressed air

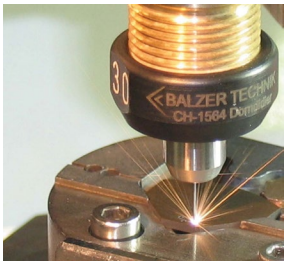

Fig. 40. SEM images of machining results of dry-ED drilling with compressed air in four different workpiece materials.

Signal analyses of the voltage u and current i as well as demanding CFD simulations of flushing processes, with compressed air and pure gases both modelled as real gases, allow for detailed insights in the complex processes within the working gap, Fig. 41. Despite the highly complex thermodynamic processes, the model validation by means of pressure measurements showed only minor deviations between measurement and simulation in the range of $10\ \% < \Delta p < 15\%$, giving credibility to local as well as general gas dynamic effects [90]. Independent of the dielectric medium, from the flushing pressure p_f at position P_0 to the bottom of the borehole at P_3, severe pressure losses occur in the order of 99 %, resulting in a pressure p that is still around 2.5 times higher for argon compared to liquid dielectrics for the tool electrode configuration in Fig. 41. In the whole working gap, the velocity c of the gases is 100 times higher compared to liquids. Despite these high velocities c, the flushing efficiency I_f of the gases, defined as the specific flushing momentum P_f, is at least two times lower than that of liquid dielectrics, Fig. 41. In dependence of the flushing configuration, this difference increases up to a factor of ten [90]. The reason for this is the 40 to 50 times lower dynamic viscosity η of the gases, which results in only a small specific flushing momentum P_f being transferred to debris particles. Especially at the bottom of the borehole it is additionally reduced due to the strong temperature decrease caused by the gas expansion. Argon, air and nitrogen have a flushing efficiency I_f that is more than two times higher than that of oxygen or helium. The removal and wear behavior observed experimentally can therefore not be described with the flushing conditions of the dielectrics alone. Parameters such as the breakdown resistance must also be considered.

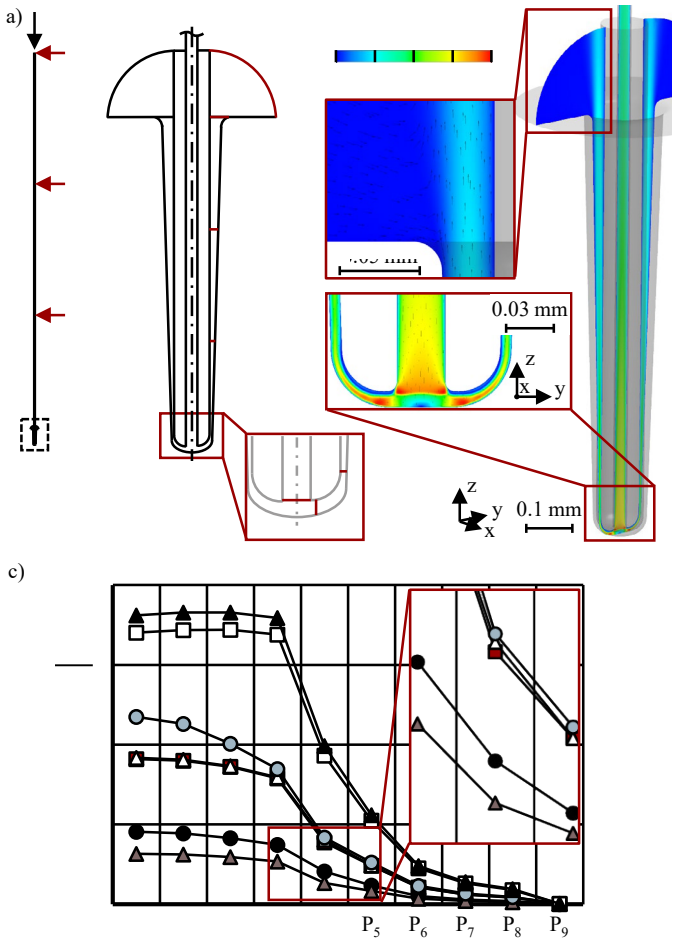

Software:
CFX 18.2, ANSYS INC., Canonsburg, USA

Tool electrode:

Electrode diameter	d_{el} =	0.10 mm
Inner diameter	d_{in} =	0.03 mm
Electrode length	l_{el} =	35.00 mm

Workpiece electrode:

Workpiece height	h =	0.90 mm

Numerical setup:

Flushing pressure	p_f =	4.00 MPa
Turbulence modeling	SST	
Equation of state (real gases)	Peng-Robinson	

▲ Water
□ IME 63 (oil)
○ Argon
△ Helium
■ Air
● Oxygen
△ Nitrogen

Fig. 41. Numerical analysis of the flushing capabilities of gaseous and liquid dielectrics; (a) simulation model and evaluation positions; (b) contour plot of the flow velocity c of air inside the working gap; (c) flushing efficiency I_f.

3. Conclusion

Within this keynote paper state-of-the-art major challenges like debris removal and related process instabilities are discussed as basis for novel advances and technical solutions within this field of research. Basic research results in machine tool development for dry-EDM, peripheral systems for automated external and inverted pressure flushing as well as for redistribution of discharges allow for short time-to-market industrialization. Approaches for tool electrode geometries and materials for sinking and drilling EDM show a great potential to overcome state-of-the-art major challenges related to debris removal and tool electrode wear. Recent results in handling, positioning and application of ultra-fine carbon fiber electrodes for drilling EDM serve as a basis for extensive basic research on process technology. The developed technologies for using gaseous dielectric fluids enable new applications for advanced EDM with advantages in terms of handling, machinable materials and gaseous related process enhancements.

The shown advances in EDM can serve as basis for further basic and applied research within the international community.

Acknowledgements

The authors would like to thank the GERMAN RESEARCH FOUNDATION (DFG) and the FEDERAL MINISTRY FOR ECONOMIC AFFAIRS AND CLIMATE ACTION (BMWK) with its project executing organization AIF PROJEKT GMBH for funding the basic research projects SPP 1476, UH100/110-3, UH100/137-3, UH100/250-1, UH100/252-1, UH100/258-1, UH100/261-1, UH100/273-1, UH100/279-1 and cooperation projects ZF4067147DF9, ZF4067142PO9, KK5051507RP1, ZF4067129RP8, that form the basis of this Keynote Paper.

References

[1] Koenig W, Dauw DF, Levy G, Panten U. EDM-Future Steps towards the Machining of Ceramics. CIRP Annals 1988;37-2:623-631.
[2] Uhlmann E, Mullany B, Biermann D, Rajurkar KP, Hausotte T, Brinksmeier E. Process chains for high-precision components with micro-scale features. CIRP Annals Manuf Techn 2016;65:549-572.
[3] Masuzawa T, Cui X, Taniguchi N. Improved Jet Flushing for EDM. CIRP Annals 1992;41;1;239-242.
[4] Klocke F, König W. Fertigungsverfahren 3. 4th ed. Berlin, Heidelberg: Springer; 2007.
[5] Uhlmann E, Polte J, Bolz R, Yabroudi S, Streckenbach J, Bergmann A. Application of additive manufactured tungsten carbide-cobalt electrodes with interior flushing channels in S-EDM. Procedia CIRP 2020;95:460-465.
[6] Pontelandolfo P, Haas P, Perez R. Particle hydrodynamics of the electrical discharge machining process. Part 2: Die sinking process. Proc CIRP 2013;6:47-52.
[7] Kliuev M, Baumgart C, Wegener K. Fluid Dynamics in Electrode Flushing Channel and Electrode-Workpiece Gap During EDM Drilling. Proc CIRP 2018;68:254-259.
[8] Kliuev M, Baumgart C, Wegener K. Fluid Dynamics in Electrode Flushing Channel and Electrode-Workpiece Gap During EDM Drilling. Procedia CIRP 2018;68:254-259.
[9] Klocke F, Schneider S, Frauenknecht B, Hensgen L, Klink A, Oßwald K. Thermographic Analysis of Spark Location Distribution in Sinking EDM. Procedia CIRP 2018;68:280-285.
[10] Kitamura T, Kunieda M, Abe K. High-speed imaging of EDM gap phenomena using transparent electrodes. Proc CIRP 2013;6:314-319.
[11] Kunieda M, Kitamura T. Observation of Difference of EDM Gap Phenomena in Water and Oil Using Transparent Electrode. Procedia CIRP 2018;68:342-346.
[12] Li G, Natsu W, Yu Z. Elucidation of the mechanism of the deteriorating interelectrode environment in micro EDM drilling. Int J Mach Tools Manuf 2021;167;103747:1-19.
[13] Kunieda M, Yoshida M, Taniguchi N. Electrical Discharge Machining in Gas. CIRP Annals 1997;46-1:143-146.
[14] Yoshida M, Kunieda M. Study on the Distribution of Scattered Debris Generated by a Single Pulse Discharge in EDM Process. Int J Elect Mach 1998;3:39-46.
[15] Roth R, Balzer H, Kuster F, Wegener K. Influence of the Anode Material on the Breakdown Behavior in Dry Electrical Discharge Machining. Proc CIRP 2012;1:639-644.
[16] Peschot A, Bonifaci N, Lesaint O, Valadares C, Poulain C. Deviations from the Paschen's law at short gap distances from 100 nm to 10 µm in air and nitrogen. Appl Phys Letters 2014;105;123109:1-4.
[17] Perfilov I. Maschine und Technologie für die Bahnerosion mit gasförmigem Dielektrikum zur Herstellung von Mikrostrukturen. In: Uhlmann E, editor. Berichte aus dem Produktionstechnischen Zentrum Berlin. Stuttgart: Fraunhofer Verlag; 2022.

[18] Wiessner M, Macedo FTB, Martendal CP, Kuster F, Wegener K. Fundamental Investigation of EDM Plasmas, Part I: A Comparison between Electric Discharges in Gaseous and Liquid Dielectric Media. Proc CIRP 2018;68:330-335.
[19] Roth R, Kuster F, Wegener K. Influence of oxidizing gas on the stability of dry electrical discharge machining process. Proc CIRP 2013;6:338-343.
[20] Uhlmann E, Polte M, Yabroudi S. Manufacturing of micro bores in high-performance materials by use of dry electrical discharge drilling. euspen SIG meeting: Micro/Nano Manufacturing, Berlin, 2019.
[21] Uhlmann E, Perfilov I, Yabroudi S, Mevert R, Polte M. Dry-ED milling of micro-scale contours with high-speed rotating tungsten tube electrodes. Proc CIRP 2020;95:533-538.
[22] Hinduja S, Kunieda M. Modelling of ECM and EDM processes. CIRP Annals 2013;62-2:775-797.
[23] Klocke F, Mohammadnejad M, Zeis M, Klink A. Investigation on the Variability of Existing Models for Simulation of Local Temperature Field during a Single Discharge for Electrical Discharge Machining (EDM). Procedia CIRP 2018;68:260-265.
[24] Kunieda M, Takaya T, Nakano, S. Improvement of Dry EDM Characteristics Using Piezoelectric Actuator. CIRP Annals Manuf Techn 2004;53:183-186.
[25] Berger T, Herzig M, Hackert-Oschätzchen M, Schulze HP, Martin A, Kröning O, Schubert A. Experimental Characterisation of a High Dynamic Piezo Module for Resource-efficient Electrothermal Precision Ablation. Procedia CIRP 2020;95:505-510.
[26] Bamberg E, Heamawatanachai S. Orbital electrode actuation to improve efficiency of drilling micro-holes by micro-EDM. Journal of Materials Processing Technology 2009;209:1,826-1,834.
[27] Fu XZ, Zhang Y, Zhang QH, Zhang JH. Research on Piezoelectric Self-Adaptive Micro-EDM. Proc CIRP 2013;6:303-308.
[28] Uhlmann E, Domingos D. Investigations on Vibration-assisted EDM-machining of Seal Slots in High-Temperature Resistant Materials for Turbine Components –Part II. Procedia CIRP 2016;42:334-339.
[29] Ichikawa T, Natsu W. Realization of Micro-EDM under Ultra-Small Discharge Energy by Applying Ultrasonic Vibration to Machining Fluid. Proc CIRP 2013;6:326-331.
[30] Goiogana M, Sarasua JA, Ramos JM. Ultrasonic Assisted Electrical Discharge Machining for High Aspect Ratio Blind Holes. Proc CIRP 2018;68:81-85.
[31] Caggiano A, Napolitano F, Teti R, Bonini S, Maradia U. Advanced die sinking EDM process monitoring based on anomaly detection for online identification of improper process conditions. Procedia CIRP 2020;88:381-386.
[32] Balzer H. Hartmetall als Werkstoff für die Bohr- und Bahnerosion, Mikroproduktion 03/15, ISSN: 1614-4538, 2015.
[33] Klocke F, Schwade M, Klink A, Veselovac D. Analysis of material removal rate and electrode wear in sinking EDM roughing strategies using different graphite grades. Procedia CIRP 2013;6:163-167.
[34] Inoue K. Multiple pipe element electrode assembly EDM method and apparatus. Property right US4441004A Publication. Inoue Japax Research Inc. Patent, 1984.
[35] Dave HK, Kumar S, Nipul CR, Harit KR. Electro discharge machining of AISI 304 using solid and bundled electrodes. Proceedings of the 26th AIMTDR 2014:296-1 - 296-7.
[36] Trych-Wildner A, Kudla L. Can carbon fibres work as tool electrodes in micro electrical discharge machining? J Micromech Microeng 2016;26:075007.
[37] Trych A. Further Study of Carbon Fibres Electrodes in Micro Electrical Discharge Machining. Proc CIRP 2013;6:309-313.
[38] Amorim F, Lohrengel A, Neubert VF, Higa C, Czelusniak T. Selective laser sintering of Mo-CuNi composite to be used as EDM electrode. Rapid Prototyping Journal 2014;20:59-684.
[39] Czelusniak T, Amorim F, Higa C, Lohrengel A. Development and application of new composite materials as EDM electrodes manufactured via selective laser sintering, Int J Adv Manuf Techn 2014;72:1,503-1,512.
[40] Tanjilul M, Senthil Kumar A. Die-sinking of super dielectric based electrical discharge machining using 3D printed electrodes. Procedia CIRP 2020;95:471-475.
[41] Yanagida D, Nakamoto T, Minami H, Miki T, Uchida S, Kimura T, Watanabe K. Electrical Discharge Machining using Copper Electrode made by Additive Manufacturing. Procedia CIRP 2020;95:449-453.
[42] Uhlmann E, Perfilov I, Schimmelpfennig TM. Open Source CNC-Maschinensteuerung für die Trockenfunkenbahnerosion. ZWF Zeitschrift für wirtschaftlichen Fabrikbetrieb 2016;111-7-8:430-433.
[43] Perfilov I, Streckenbach J, Schimmelpfennig T-M, Uhlmann E. Module for Micro Electrical Discharge Machining with Gaseous Dielectrics. In: Wulfsberg JP, Sanders A, editors. Small Machine Tools for Small Workpieces. Hamburg: Springer; 2017. p. 35-47.
[44] Uhlmann E, Perfilov I. Machine tool and technology for manufacturing of micro-structures by micro dry electrical discharge milling. Proc CIRP 2018;68:825-830.
[45] Uhlmann E, Perfilov I, Schimmelpfennig TM, Schweitzer L, Yabroudi S. Dry-EDM milling of micro-scale features with high speed rotating tungsten tube electrodes. Proc. 17th Int euspen Conf. 2017;175-176.
[46] Langmack M. Laserwendel- und funkenerosives Mikrobohren. In: Uhlmann E, editor. Berichte aus dem Produktionstechnischen Zentrum Berlin. Stuttgart: Fraunhofer Verlag; 2015.
[47] Schimmelpfennig T-M. Trockenfunkenerosives Feinbohren von Hochleistungswerkstoffen. In: Uhlmann E, editor. Berichte aus dem Produktionstechnischen Zentrum Berlin. Stuttgart: Fraunhofer Verlag; 2016.
[48] Cetin S, Okada A, Uno Y. Effect of Debris Distribution on Wall Concavity in Deep-Hole EDM. JSME Int. J. Series 2004;C47-2:553-559.
[49] Nastasi R, Koshy P. Analysis and performance of slotted tools in electrical discharge drilling. CIRP Annals Manuf Techn 2014;63:205-208.
[50] Uhlmann E, Polte M, Streckenbach J, Dinh NC, Börnstein J. Inverted pressure flushing for drilling EDM. euspen SIG meeting: Micro/Nano Manufacturing, Berlin, 2019.
[51] Dinh NC, Hörl R, Yabroudi S. Reducing the Number of CFD Computer Experiments by Use of Latin Hypercube Design and Kriging Regression on the Example of Side Flushing in Sinking EDM. Production at the Leading Edge of Technology. 2021:151-159.
[52] Makenzi MM, Ikua BW. A review of flushing techniques used in electrical discharge machining. Mech Eng Conf Sust R Innov 2012;4:162-165.
[53] Uhlmann E, Polte M, Streckenbach J, Becker T, Thißen K, Bolz R. Segmentierte Werkzeugelektroden. wt-Werkstattstechnik online 2021;7/8:501-507.
[54] Uhlmann E. Grundlagen zum Abtragen. In: Heisel U, Klocke F, Uhlmann E, Spur G, editors. Handbuch Spanen. München: Hanser; 2014. p. 1,127-1,140.
[55] Rechenberg I. Evolutionsstrategie ´94. Stuttgart: Frommann-Holzboog; 1994.
[56] Streckenbach J, Santibáñez Koref I, Rechenberg I, Uhlmann E. Optimization with the evolution strategy by Example of Electrical-Discharge Drilling. In: Pérez García H, Alfonso-Cendón J, Sánchez González L, Quintián H, Corchad E, editors. Conf Proc Int Joint Conf SOCO'17-CISIS'17-ICEUTE'17. Cham: Springer; 2018. p. 125-136.
[57] Streckenbach J, Santibáñez Koref I, Rechenberg I, Uhlmann E. Optimization with the evolution strategy by example of electrical-discharge drilling. Neurocomp 2020;391:318-324.
[58] Hansen N. The CMA Evolution Strategy: A Comparing Review. In: Lozano JA, Larrañaga P, Inza I, Bengoetxea E, editors. Towards a New Evolutionary Computation. Studies in Fuzziness and Soft Computing, vol. 192, Berlin, Heidelberg: Springer; 2006. p. 75-102.
[59] Uhlmann E, Streckenbach J, Thißen K, Schulte Westhoff B, Masoud A, Maas J. Concept for an actuated variable tool electrode for use in sinking EDM. Proc. 21th Int euspen Conf. 2021;183-184.
[60] Schulte Westhoff B, Maas J. Modeling and Control of Miniaturized Electric Linear Drive with Two-phase Current Excitation. IEEE/ASME Int Conf Adv Intell Mechatr 2021:332-337.
[61] Uhlmann E, Thißen K, Schulte Westhoff B, Streckenbach J, Ludwig J, Maas J. Process behaviour of segmented and actuated tool electrodes for variable shaping in sinking EDM. Proc. 22nd Int euspen Conf. 2022;t.b.a.. (not yet published)
[62] Plaza S, Sanchez JA, Perez E, Gil R, Izquierdo B, Ortega N, Pombo I. Experimental study on micro EDM-drilling of Ti6Al4V using helical electrode. Prec Eng 2014;38:821-827.

[63] Wang K, Zhang Q, Zhu G, Liu Q, Huang Y. Experimental study on micro electrical discharge machining with helical electrode. Int J Adv Manuf Technol 2017;93:2,639-2,645.
[64] Kumar R, Singh I. Productivity improvement of micro EDM process by improvised tool. Prec Eng 2018;51:529-535.
[65] Kumar R, Singh I. A modified electrode design for improving process performance of electric discharge drilling. J Mat Proc Tech 2019;264:211-219.
[66] Uhlmann E, Yabroudi S, Perfilov I, Schweitzer L, Polte M. Helical electrodes for improved flushing conditions in drilling EDM of MAR-M247. Proc. 18th Int euspen Conf. 2018;415-417.
[67] Yabroudi S. Einsatzbewertung neuartiger Werkzeugelektroden mit außenliegenden Spülkanälen beim funkenerosiven Bohren mittels CFD Simulationen. 37th CADFEM ANSYS Sim Conf 2019.
[68] Thißen K, Streckenbach J, Santibáñez Koref I, Polte M, Uhlmann E. Signal analysis on a single board computer for process characterisation in sinking electrical discharge machining. In: Behrens BA, Brosius A, Drossel WG, Hintze W, Ihlenfeldt S, Nyhuis P, editors. Production at the Leading Edge of Technology. WGP 2021. Berlin: Springer; 2021. p. 169-176.
[69] Czelusniak T, Fernandes Higa C, Torres RD, Laurindo CAH, Fernandes de Palva Junior JM, Lohrengel A, Amorim FL. Materials used for sinking EDM electrodes: a review. J Braz Soc Mech Sc Eng 2019;41:14.
[70] Uhlmann E, Polte, M, Bolz R, Börnstein J. Fundamental research of applying tungsten carbide-cobalt as tool electrode material for sinking EDM. Procedia CIRP 2020;95:466-470.
[71] Bleys P. Electrical Discharge Milling: Technology And Tool Wear Compensation. Dissertation, Katholieke Universiteit Leuven, 2003.
[72] Maradia U, Wegener K, Stirnimann J, Knaak R, Boccadoro M. Investigation of the scaling effects in meso-micro EDM. Proceedings of the ASME International Mechanical Engineering Congress and Exposition 2013;IMECE2013-63160.
[73] Uhlmann E, Domingos DC. Automated dressing of graphite electrodes for electrical discharge machining (EDM) of seal slots in turbine components. Procedia Manufacturing 2016;6:45-52.
[74] Kunieda M, Lauwers B, Rajurkar KP, Schumacher BM. Advancing EDM through Fundamental Insight into the Process. CIRP Annals Manuf Techn 2005;54:64-87.
[75] Uhlmann E, Bergmann A,Bolz R. Application of additive manufactured tungsten carbide tool electrodes in EDM. Procedia CIRP 2018;68:86-90.
[76] Uhlmann E, Oberschmidt D, Bolz R. Application of Micro Structured, Boron Doped CVD-diamond as µEDM Tool Electrodes, Procedia CIRP 2018;68:649-653.
[77] Uhlmann E, Polte M, Streckenbach J. Surface modified tool electrodes for optimized drilling EDM. Special Interest Group Meeting: Micro/Nano Manufacturing. 2019.
[78] Uhlmann E, Polte M, Streckenbach J. Oxidized tool electrodes for optimized electro-discharge drilling. Proc. 20th Int euspen Conf. 2020;145-146.
[79] Uhlmann E, Polte M, Streckenbach J. Application of tool electrodes oxidised with humid and dry air during the electro-discharge drilling of MAR-M247 alloy. Proc. 21th Int euspen Conf. 2021;191-192.
[80] Dies K. Kupfer und Kupferlegierungen in der Technik. Berlin, Heidelberg: Springer; 1967.
[81] De Los Santos Valladares L et al.. Crystallization and electrical resistivity of Cu2O and CuO obtained by thermal oxidation of Cu thin films on SiO2/Si substrates. Thin Solid Films 2012;520-20:6,368-6,374.
[82] Sodick Co., Ltd.: Linear Motor Technology. September 29, 2005:39.
[83] Egashira K, Morita Y, Hattori Y. Electrical discharge machining of submicron holes using ultrasmall-diameter electrodes. Prec Eng 2010;34:139-144.
[84] Uhlmann E, Piltz S, Doll U. Machining of micro/miniature dies and moulds by electrical discharge machining—Recent development. Journal of Materials Processing Technology 2005;167:488-493.
[85] Uhlmann E, Röhner M, Langmack M. Micro-EDM. In: Qin Y, editor. Micromanufacturing Engineering and Technology. Oxford: Elsevier; 2010. p. 39-58.
[86] Egashira K, Masuzawa T. Microultrasonic Machining by the Application of Workpiece Vibration. Annals ClRP 1999;48-1:131-134.
[87] Pham DT, Dimov SS, Bigot S, Ivanov A, Popov K. Micro-EDM - recent developments and research issues. J Mat Proc Tech 2004;149:50-57.
[88] Uhlmann E, Polte M, Haesche T, Yabroudi S. Development of a handling system for single carbon fibres as tool electrodes in micro EDM. euspen SIG Meeting: Micro/Nano manufacturing, 2021.
[89] Uhlmann E, Perfilov I, Yabroudi S, Schweitzer L, Polte M. Electro-discharge drilling with MP-based carbon fibre electrodes. Proc. 18th Int euspen Conf. 2018;417-419.
[90] CFD-Simulation in Mikrospülkanälen beim funkenerosiven Feinbohren mit flüssigen und gasförmigen Dielektrika. 35th CADFEM ANSYS Sim Conf 2017.
[91] Uhlmann E, Schimmelpfennig T, Perfilov I, Streckenbach J, Schweitzer L. Comparative Analysis of Dry-EDM and Conventional EDM for the Manufacturing of Micro Holes in Si_3N_4-TiN. Proc CIRP 2016;42:173-178.